

¹

José D. Ruiz-Álvarez

²

Compiled on 26/05/2015 at 01:52

⁵ **Outline**

1 The Standard Model

Since the Greeks, different theories about the composition and structure of the world have been formulated. At ancient Greece these theories were elaborated from a philosophical point of view. Nowadays, we count with a very sophisticated set of tools and concepts that allowed us to build up a general vision of nature, its components and structure. Moreover, on the subject of the constituents, or elemental constituents, a theory capable of describing the majority of known phenomena has been developed. This theory is the Standard Model (SM) of particle physics.

This SM relies in two of the more elegant constructs of modern physics and mathematics. From the physics side, the quantum field theory; from mathematics, group theory. Quantum field theory has born from the understanding of processes that take place at very small spatial scales and in a regime where special relativity play an important role. To describe such, a major part of the most brilliant minds of the 20th century dedicated their life, Paul Dirac, Richard Feynman, Enrico Fermi among them. The theory of quantum fields has set in a common place two extraordinary achievements of physics: special relativity and quantum mechanics. With it we have been capable to describe many phenomena: β and α decay, solid state, among many other.

From the mathematics side, group theory has become one of the most powerful tools for particle physicist. However, their development began quite early, with Galois around 1830, and was used in other parts of physics, it's with Lie algebras and the possibility of describing continuous symmetries that the most important step were given. Also, this would have not been possible with the amazing connection found by Emmy Noether in 1918. She found that for every conserved quantity there is a preserved symmetry. Group theory can be seen, roughly speaking, a way to mathematically describe symmetries, group theory became the tool to describe systems with conserved quantities.

In this chapter, we present the basics of the SM. We describe its seminal ideas, its structure and content and its ultimate consequences. Finally, we close with its limitations.

³⁷ 1.1 Fields, symmetries and interactions

³⁸ From the very beginning of physics, one of the most fundamental questions has
³⁹ been how does bodies interact, and what is exactly an interaction. On the first
⁴⁰ type of interaction ever studied by physics, gravity, Newton proposed the con-
⁴¹ cept of distant interaction, the idea that bodies could interact without being in
⁴² direct contact. But the question on how exactly that distant action was performed
⁴³ remained unanswered.

⁴⁴ During the 19th and 20th century new phenomena were discovered pointing to
⁴⁵ brand new interactions, electricity, magnetism and radioactivity. The very precise
⁴⁶ and complete description of electromagnetism developed by Gauss, Faraday, Am-
⁴⁷ père and finished by Maxwell arrived to describe electricity and magnetism under
⁴⁸ the formalism of only one interaction within the mathematical formalism of classi-
⁴⁹ cal fields. Further works addressed radioactivity, driving to a deeper understanding
⁵⁰ of nature and its composition.

⁵¹ For the following discussion, and later, we are going to work in natural units
⁵² for simplicity. In these units the speed of light c is normalized to unity, as well as
⁵³ electron electric charge e , reduced Planck constant \hbar and Boltzmann constant k_B .
⁵⁴ Then, masses and temperature are expressed in energy units, i.e. eV , and time
⁵⁵ and length in inverse energy units, eV^{-1} .

⁵⁶ A classical field is an assignment of a quantity to every point in space and time.
⁵⁷ For physics, the quantity that is attributed is a physical quantity such as mass,
⁵⁸ electrical charge or probability. This quantity can be scalar or vector, giving rise to
⁵⁹ the notion of scalar or vector field, correspondingly. The simplest example, is the
⁶⁰ temperature in a gas, that is a scalar quantity assigned to every point. Another
⁶¹ example, a fluid can be described in terms of fields, being the velocity of the fluid
⁶² a vector field and its pressure a scalar field. Generic classical electromagnetic
⁶³ interactions can be described with the help of one vector field $\vec{A}(x)$, the vector
⁶⁴ potential, and one scalar field $\phi(x)$, the scalar potential. In the formalism of
⁶⁵ four-vectors from relativistic dynamics one can organize these two quantities in the
⁶⁶ four-potential $A_\mu = (-\phi, \vec{A})$. This can be used to define the strength field tensor
⁶⁷ $F_{\mu\nu} = \partial_\mu A_\nu - \partial_\nu A_\mu$, where $\partial_\mu = \left(-\frac{\partial}{\partial t}, \nabla\right)$ is the covariant derivative. From the
⁶⁸ tensor is possible to obtain in a very generic and elegant way the equations of
⁶⁹ motion of the free field using the Lagrangian formalism, as in equation 1.1. With
⁷⁰ the Lagrangian density defined in equation 1.2.

$$\partial_\mu \left(\frac{\partial \mathcal{L}}{\partial(\partial_\mu A_\nu)} \right) - \frac{\partial \mathcal{L}}{\partial A_\nu} = 0 \quad (1.1)$$

$$\mathcal{L} = -\frac{1}{4} F^{\mu\nu} F_{\mu\nu} \quad (1.2)$$

71 It's very important to notice that the equations of motion of the free field are
 72 invariant under the choice of the four-potential. More precisely, the covariant
 73 potential is not unique and we can always add the covariant derivative of a scalar
 74 field,

$$A'_\mu = A_\mu + \partial_\mu \Lambda(x) \leftrightarrow \partial^\mu A_\mu = 0 \quad (1.3)$$

75 and describe the same physics. This non-uniqueness corresponds to the choice
 76 of a zero-point of the potential very well known in non-Lagrangian formalism of
 77 electrodynamics. When we choose a specific value for this scalar field, $\Lambda(x)$, we
 78 say that the gauge has been fixed.

79 One can also define a four current vector, $J_\mu = (\rho, \vec{J})$ with ρ the electric charge
 80 density and \vec{J} the current charge density. Then, plugging in this four current in
 81 the Lagrangian of the free field, defined in equation 1.2,

$$\mathcal{L} = -\frac{1}{4} F^{\mu\nu} F_{\mu\nu} - A_\mu J^\mu \quad (1.4)$$

82 we can obtain the complete set of equations of motion of the field with charges
 83 and currents.

84 The transformation stated from equation 1.3 can be understood as a transfor-
 85 mation of the field. These type of transformations are mathematically understood
 86 under the group $U(1)$, where the generic transformation operator can be written
 87 as $U = e^{i\theta(x)}$. It's said then that the electromagnetic vector potential is *invariant*
 88 under $U(1)$ transformations. This property identifies an essential characteristic of
 89 electromagnetism, its symmetric behavior under $U(1)$.

90 From this reasoning the most interesting results are drawn when the same sym-
 91 metry is imposed to another fields. For example, the kinetic Lagrangian for a
 92 complex scalar field is $\mathcal{L} = (\partial^\mu \phi)^* \partial_\mu \phi$. To perform the transformation on the
 93 scalar field, it is sufficient to apply the operator as $\phi' = U\phi$ and $\phi'^* = \phi^* U^{-1}$. But
 94 it's evident that the Lagrangian is not the same after applying such transforma-
 95 tion. Then, in order to preserve the Lagrangian under $U(1)$ is necessary to change
 96 at the same time the derivative. Such transformation is given in equation 1.5,
 97 where g is a constant.

$$\mathcal{D}^\mu = \partial^\mu - ig A^\mu \quad (1.5)$$

98 Then, the proposed Lagrangian can be rewritten, including the vector field, as

$$\mathcal{L} = (\mathcal{D}^\mu \phi)^* \mathcal{D}_\mu \phi - \frac{1}{4} F^{\mu\nu} F_{\mu\nu} \quad (1.6)$$

99 that is invariant under $U(1)$. An interaction term, of the form $ig A^\mu \phi^* \partial_\mu$, between
 100 the scalar and the vector field, can be derived from the kinematic part of the
 101 Lagrangian $\mathcal{D}^\mu \phi)^* \mathcal{D}_\mu \phi$. This shows that the requirement of the invariance under

102 103 104 105 106 107 $U(1)$ of the scalar field lead to the introduction of an interaction with a vector field controlled by the constant g . We have also seen that electromagnetic interaction is described precisely by a vector field and that preserves $U(1)$ symmetry, which implies that this symmetry is the connection to electromagnetic interaction, identifying the interaction itself with the $U(1)$ symmetry. In addition, using Noether theorem one can show that g is a conserved quantity, as the electric charge is.

108 109 110 111 112 113 114 115 116 117 But not only electromagnetism can be described via a continuous symmetry as $U(1)$. On 1896 radioactivity was discovered by the french physicist Henri Becquerel. Three years after, Marie and Pierre Curie studied in more detail the phenomenon and found Polonium and Radium elements. And later on, Ernst Rutherford was able to describe radioactivity as coming in three types, alpha (α), beta (β) and gamma (γ). He also noticed that radioactivity was able to change matter, which allowed him, with also other experiences, to propose an atomic model, describing elements as basically an external core of negative charges and a nucleus positively charged. Consequently, This findings implied the existence of interactions different to electromagnetism, acting at the atomic scale.

118 119 120 121 122 123 The interaction that undergoes radioactivity, beta decay, is called the weak interaction. In 1933 Enrico Fermi made a first theoretical description of this interaction, but only in 1968 Sheldon Glashow, Abdus Salam and Steven Weinberg were able to describe weak interaction with a symmetry group: $SU(2)$. Finally, the interaction that keeps the nucleus components together, the strong interaction, was described with $SU(3)$ group mainly by Murray Gell-Mann in 1963.

124 125 126 There have been many attempts to describe gravity with the same formalism, but up to present such attempts have been unsuccessful. Such question remains one of the most important problems for modern particle physics.

127 1.2 Quantum fields and particles

128 129 130 131 132 Classical fields, introduced and described in last section 1.1, can be extended to a quantum theory. Such procedure is known as the quantization of fields and allow to unify special relativity and quantum mechanics in one theory, Quantum Field Theory (QFT), to describe the dynamics of systems in such regimes: speed close to the speed of light on the atomic or smaller scales.

133 134 135 136 137 138 139 Quantum mechanics introduced two fundamental concepts: first, the description of the system by its states; and second, the identification of an observable with an operator. The state of a system is identified with a set of quantum numbers that tell us the characteristics of the system when it is at some state. For example, the hydrogen atom system has energy as quantum number, such that each state has a value for the energy describing the potential energy contained in the system. Quantum states are mathematically noted in Dirac notation as a *ket*,

$$|\alpha\rangle = |i, j, k, \dots\rangle \quad (1.7)$$

with α the set of quantum numbers i, j, k, \dots . This mathematical object lives in Hilbert space (a complex space \mathbb{C} of functions), which conjugate, a *bra*, is noted $\langle\alpha|$, and their internal product $\langle\beta|\alpha\rangle$. The numerical value of $|\langle\beta|\alpha\rangle|^2$ gives the transition probability of the system from state β to state α , and $|\langle\alpha|\alpha\rangle|^2$ is the probability to find the system in state the α .

Physical observables as position, energy or momentum are described by complex operators such that to measure their value for a given state, one just have to calculate $|\langle\alpha|\hat{O}|\alpha\rangle|^2$. The identification of observables and operators is called *first quantization*. In addition, Schrodinger equation describes the evolution of states,

$$\hat{\mathcal{H}}|\alpha\rangle = i\frac{d}{dt}|\alpha\rangle \quad (1.8)$$

with \mathcal{H} the Hamiltonian of the system. The whole formalism is able to explain *quantized* systems, where the quantum numbers are discrete, such as hydrogen atom or black body.

Several functions or fields can be related to a given state. These functions, wave functions, can be used as the states to calculate probabilities. In *second quantization* wave functions are upgraded into field operators. This procedure gives rise to the quantization of the state of the field, which is described by the quantum number n which is definite positive. $n = 0$ for the fundamental state and $n > 0$ for the excited states. Such excitations of the field are understood as physical particles that propagates in space-time, which means that $n = 0$ is vacuum.

The first QFT ever created was born from the quantization of the electromagnetic field. Quantum Electro Dynamics (QED) is the quantized version of classical electrodynamics, that was developed by Tomonaga, Schwinger and Feynman around 1960. This theory describes electromagnetic interactions of a charged field and the electromagnetic vector field. The charged field excitations correspond to electrons and the excitations of the vector fields are photons, responsible of light. Electrons are a particle with negative electric charge and orbit around the nucleus in atoms. Discovered in 1897 by J. J. Thomson, it was fully described by P. A. Dirac in 1928 with the Dirac equation that is the Schrodinger equation for a relativistic particle of spin $1/2$. Spin, the intrinsic angular momentum carried by a particle, can be integer $(0, 1, 2, \dots)$ or semi-integer $(\frac{1}{2}, \frac{3}{2}, \dots)$. The particles with semi-integer spin, as electrons, are called *fermions* and particles with integer spin, as photons, are called *bosons*. Dirac equation predicted the existence of a particle identical to the electron but with positive charge, the positron. It was discovered on 1932 by Carl David Anderson.

175 Up to present days we have found 12 fundamental fermions and 5 fundamental
 176 bosons. Fermions are organized in *leptons*, that don't interact strongly, and *quarks*,
 177 that do interact strongly. Leptons are as well organized in three families, the
 178 electron (e^-) and electron neutrino (ν_e), muon (μ^-) and muon neutrino (ν_μ) and
 179 tau (τ) and tau neutrino (ν_τ). Electron, muon and tau are electrically charged
 180 while neutrinos are neutral. Their respective anti-particles are equally organized,
 181 positron (e^+) with electron anti-neutrino ($\bar{\nu}_e$), anti-muon (μ^+) with muon anti-
 182 neutrino ($\bar{\nu}_\mu$) and anti-tau (τ^+) with tau anti-neutrino ($\bar{\nu}_\tau$). Quarks also come in
 183 three families, with the respective anti-quarks: up (u, \bar{u}) and down (d, \bar{d}), charm
 184 (c, \bar{c}) and strange (s, \bar{s}), top (t, \bar{t}) and bottom (b, \bar{b}). The fundamental bosons
 185 are the photon (A), the W (positively and negatively charged) and Z that mediate
 186 the electroweak interaction, the gluon (g) mediating the strong interaction and
 187 the Higgs (H). The weak bosons were discovered at CERN in 1983 at the UA1
 188 and UA2 collaborations over the SPS accelerator (described on section 2.1.1). The
 189 Higgs boson has been discovered recently on 2012 by ATLAS and CMS experiments
 190 at the LHC. The 2013 physics Nobel prize was awarded to Francois Englert and
 191 Peter W. Higgs "for the theoretical discovery of a mechanism that contributes to
 192 our understanding of the origin of mass of subatomic particles, and which recently
 193 was confirmed through the discovery of the predicted fundamental particle, by the
 194 ATLAS and CMS experiments at CERN's Large Hadron Collider".

195 **1.2.1 The mass problem**

196 Using the concepts developed on later sections about QFT and symmetries it's
 197 possible to construct a whole theory giving rise to a precise description of particles
 198 and interactions between them. But such a theory does not allow to have massive
 199 bosons, whereas masses for fermions are allowed. A mass term for a fermion ψ is
 200 of the form

$$m_\psi \bar{\psi} \psi$$

201 where m_ψ is the mass of the field.

202 Under $U(1)$ transformations, $\psi' = U\psi$, the mass term remains the same, what
 203 means that is invariant under $U(1)$ transformations. The same is not true for a
 204 boson. A mass term for a boson A , can be written as

$$m_A A^\mu A_\mu \quad (1.9)$$

205 where m_A is its mass.

206 The $U(1)$ transformation for the boson is $A'^\mu = A^\mu + \delta^\mu \theta(x)$. Applying such
 207 transformation on the mass term 1.10 one can obtain the transformed term

$$m_A (A^\mu A_\mu + A^\mu \delta_\mu \theta(x) + \delta^\mu \theta(x) A_\mu + \delta^\mu \theta(x) \delta_\mu \theta(x)) \quad (1.10)$$

where the last three terms make this term not invariant under $U(1)$ transformations. Consequently, one can say that a mass term for the boson destroy the invariance of the theory under $U(1)$ symmetry.

Nonetheless there is no need for a theory of a massive photon, there is a need to have massive bosons for weak interactions. There is a relation between the mass of a boson and the range of the interaction mediated by it. Massless bosons transmit long range interactions, as electromagnetism, but short range interactions, as the weak interaction, are mediated by massive bosons. More precisely the interaction range is inversely proportional to the mass of the boson, higher the mass shortest the range. Such relation can be seen from the structure of the propagator, which is a mathematical entity that describes the probability a particle has to travel a distance in a given time. Such propagator, for a vector boson, has a generic form given in equation 1.11, where k_μ is the momentum carried by the boson. It's clear from this structure that a massive boson has less probability to travel a long distance than a massless boson in a given time.

$$\frac{g_{\mu\nu}}{k^2 - m^2 + i\epsilon} \quad (1.11)$$

Then, as massive bosons are requires for weak interaction, somehow the $SU(2)$ symmetry has to be broken. There are basically two ways to broke a symmetry:

- Explicit symmetry breaking: By the introduction of a symmetry breaking term in the Lagrangian, as a mass term for the bosons.
- Spontaneous symmetry breaking: When the ground state of one field fail to be invariant under the symmetry.

Explicit symmetry breaking is not an option, because the symmetry needs to be preserved in the Lagrangian in order to introduce the interaction.

1.2.2 Spontaneous Symmetry Breaking

Several physical systems exhibit an spontaneous symmetry breaking. For example, a pencil balanced on its tip is perfectly symmetric system around the vertical axis, however, because of the instability of the system the pencil will eventually fall over. The final state is stable but not symmetrical. This transition also decreased the potential energy of the system, driving the system to its ground state. This means that whereas the system had a symmetry the ground state does not show the symmetry. In general, symmetry breaking is linked to phase transitions, as liquid to gas transition or magnetization of a ferromagnet, covering a plethora of

240 physical processes. To a greater extent, in recent studies, [8], the emergence of life
 241 has been understood as a phase transition of matter.

242 To achieve an spontaneous symmetry breaking of $SU(2)$ in QFT one should
 243 choose a field for which its ground state, vacuum, will fail the symmetry. This
 244 means, in practical terms, that such field will have a non-zero value in vacuum,
 245 leading to a presence of particles coming from the field on theory vacua. If a
 246 fermion field is chosen, the vacuum will show a preference on directionality de-
 247 pending on its spin orientation, what breaks Poincaré symmetry imposed by spe-
 248 cial relativity. The same is true if a spin-1 bosonic field is chosen for the task. In
 249 order to avoid this problem a spin-0 field should be used. In addition, this field
 250 should be electrically neutral to avoid having a charged vacuum.

251 Whit all this properties in mind, taking a scalar doublet of $SU(2)$, defined on
 252 equation 1.12 where ϕ^0 and ϕ^+ are complex fields, the most general potential can
 253 be written from two auto-interaction terms, in equation 1.13.

$$\Phi = \begin{pmatrix} \phi^+ \\ \phi^0 \end{pmatrix} = \begin{pmatrix} \phi^+ \\ \phi_{RE} - i\phi_{IM} \end{pmatrix} \quad (1.12)$$

$$V(\Phi) = \mu^2 \Phi^\dagger \Phi + \lambda (\Phi^\dagger \Phi)^2 \quad (1.13)$$

254 Such potential has a unique minimum for $\lambda > 0$ and $\mu^2 > 0$, but for $\lambda > 0$ and
 255 $\mu^2 < 0$ has a set of minima with the shape of “Mexican hat”, shown in figure 1.1.
 256 Under $\lambda > 0$, $\mu^2 < 0$ configuration the field breaks spontaneously the symmetry
 257 reaching the ground state, acquiring an expectation value on vacuum different
 258 from zero, v .

259 1.2.3 Englert-Brout-Higgs mechanism

260 After the spontaneous symmetry breaking, the scalar doublet transforms into the
 261 form given in equation 1.14, where G^+ and G^0 are the Goldstone bosons product
 262 of the breaking of the $SU(2)$ symmetry, and H is the Englert-Brout-Higgs boson.
 263 From Goldstone’s theorem when a symmetry is spontaneously broken a massless
 264 boson appear for each broken generator. In our specific case, the three generators
 265 of $SU(2)$ are broken giving rise to three Goldstone bosons: G^+ , G^- and G^0 . This
 266 massless bosons are “eaten” by the W^+ , W^- and Z^0 giving them an additional
 267 degree of freedom, the longitudinal polarization.

$$\Phi = \begin{pmatrix} G^+ \\ \frac{1}{\sqrt{2}}(H + v - iG^0) \end{pmatrix} \quad (1.14)$$

268 By this mechanism, the W and Z bosons acquire mass, being its value set by the
 269 coupling constant of $SU(2)$ group and the vacuum expectation value of Englert-

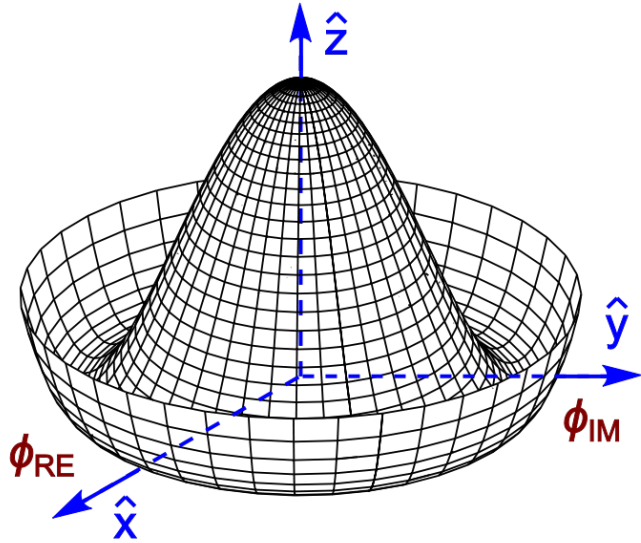


Figure 1.1: Higgs potential

270 Brout-Higgs boson. In addition, the fermions on the theory also acquire a mass
271 from the interactions with the scalar doublet. Such masses are in general of the
272 form $m_f = \lambda_f v / \sqrt{2}$, where λ_f sets the interaction between the Englert-Brout-
273 Higgs boson and the fermion. Finally, also the Englert-Brout-Higgs boson has a
274 mass $m_H^2 = -2\mu^2$.

275 In summary, with this mechanism the weak interaction bosons and fermions of
276 the theory are given a mass on the price of introducing an additional scalar field
277 to spontaneously break the $SU(2)$ symmetry.

278 1.3 Top production at LHC

279 Discovered in 1995 by DØ and CDF collaborations at Tevatron, it's the heaviest
280 fundamental particle known. As heaviest particle, many models beyond the SM
281 predict a coupling of the top quarks with a heavier new physics sector. It forms
282 a $SU(2)_L$ weak isospin doublet with the b-quark, discovered in 1977. Their mass
283 difference, two orders of magnitude, is one fundamental question in the SM. Pre-
284 cision measurements of the top quark are fundamental input to test the SM and
285 possibly find new physics.

286 The LHC can be seen as a top-factory, being the accelerator where the most of
287 top-quarks can be produced. During run 1, taking into account 7 TeV and 8 TeV
288 data, 5.6 millions of top pairs events and 2.7 millions of single top events were

289 delivered by the LHC to CMS and ATLAS experiments. Taking into account the
290 different cross sections of the production processes, that will be discussed in 1.3.1
291 and 1.3.2, and the instantaneous luminosity, cited in table 2.1.2, for 8 TeV center
292 of mass energy, at LHC there are produced around 6 tops per second where 5 of
293 them come from top-pair events and one from single-top events.

294 **1.3.1 Pair production**

295 Description of pair production and the relative importance of each channel.

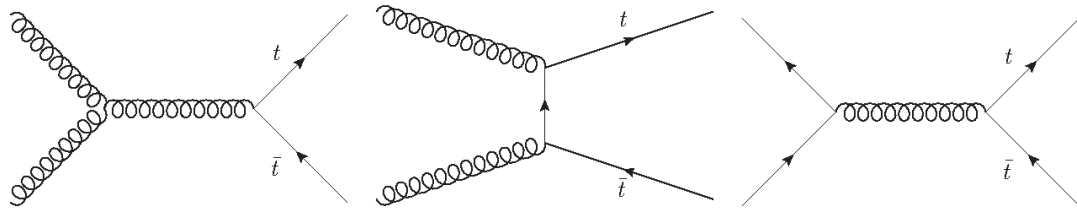


Figure 1.2: Top pair production processes Feynman diagrams for proton-proton collisions, via gluon fusion and quark-antiquark annihilation

296 **1.3.2 Single t production**

297 Description of single production and the relative importance of each channel.

298 **1.3.3 Decay channels**

299 Description of possible decays of top-quark to show different channels of searches.

300 **1.3.4 Top properties**

301 Description of top properties and the measurement of them.

302 **Electric charge**

303 Top charge related to its decay.

304 **Lifetime**

305 Discussion on the importance of measurements of top as only quark decaying before
306 hadronization time.

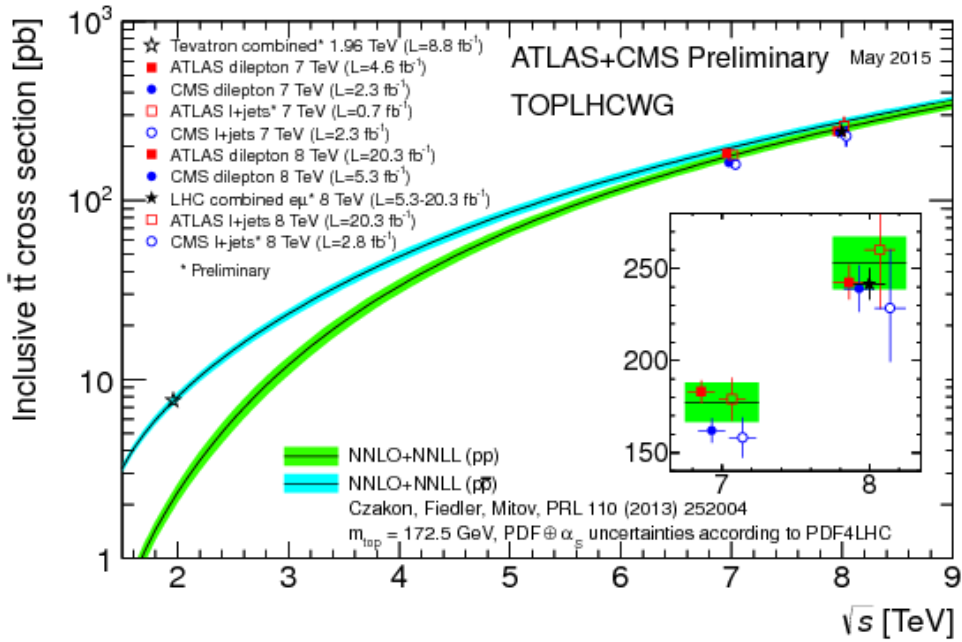


Figure 1.3: $t\bar{t}$ production cross section as function of the center of mass energy in $p\bar{p}$ and pp collisions compared to theoretical predictions.

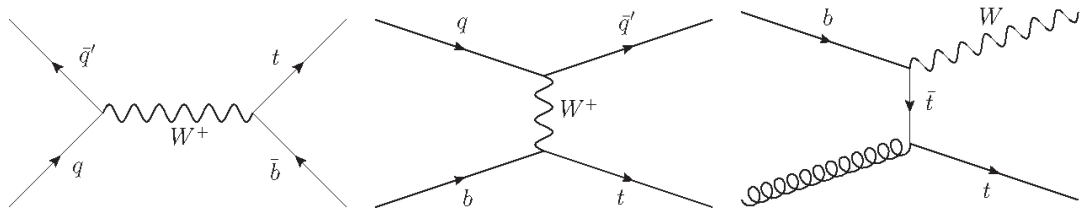


Figure 1.4: Single top production processes Feynman diagrams for proton-proton collisions, from left to right s-channel, t-channel and associated W production.

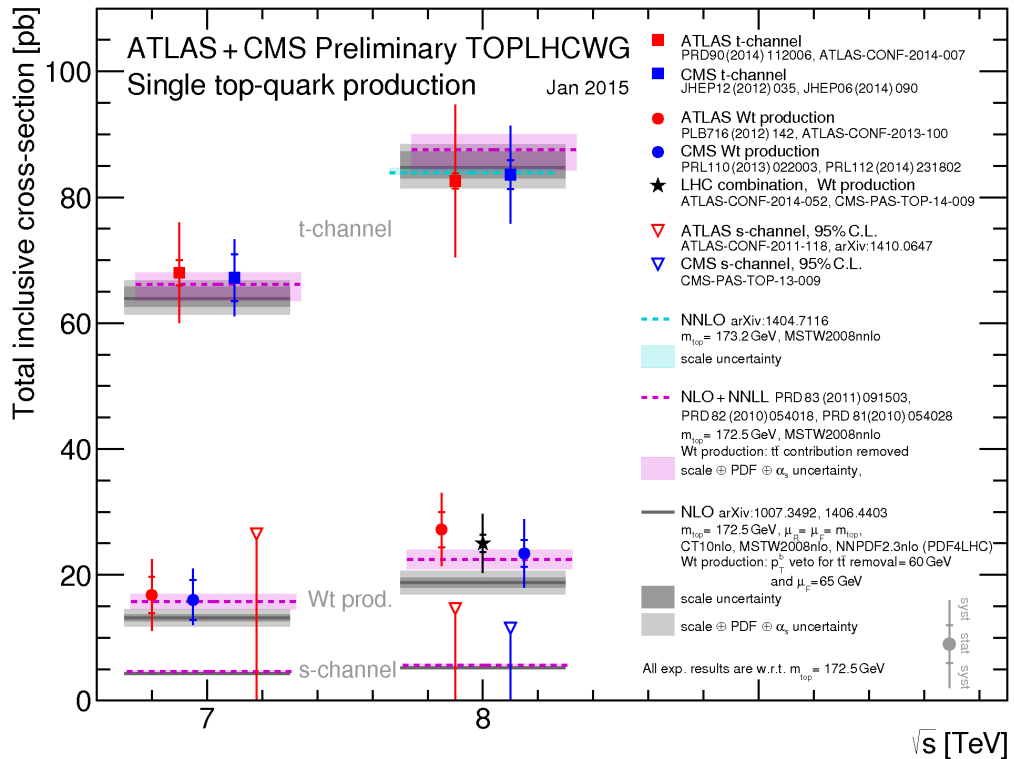


Figure 1.5: Single top production cross section as function of the center of mass energy in pp collisions compared to theoretical predictions for each production channel by ATLAS and CMS collaborations.

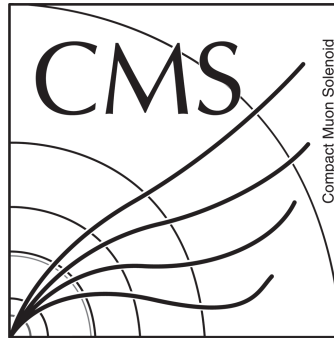


Figure 1.6: Feynman diagrams for top decay channels with respective branching ratios.

307 **Mass and width**

308 Measurements of top mass and width.

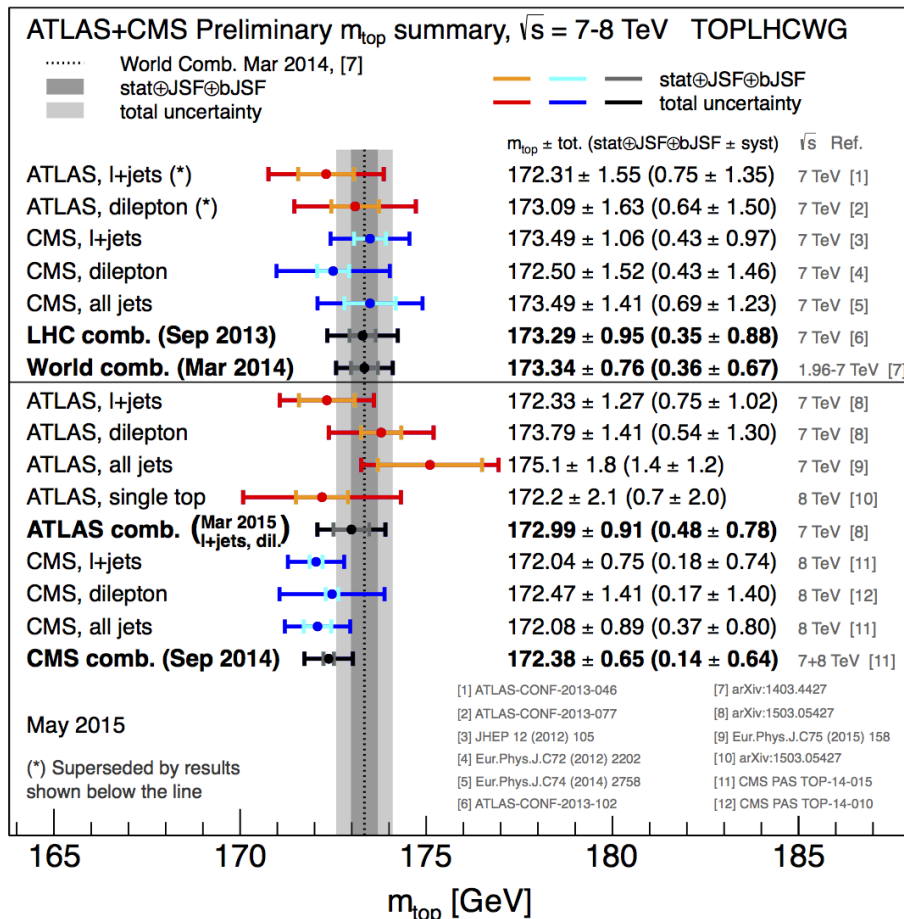


Figure 1.7: Top mass measurements from ATLAS and CMS collaborations and world combination including Tevatron results.

309 **Spin correlation**

310 Discussion on how $t\bar{t}$ system have spin correlation that will be important for
311 precision measurements.

312 1.4 Higgs production at LHC

313 Discussion of Higgs production channels and relative importance.

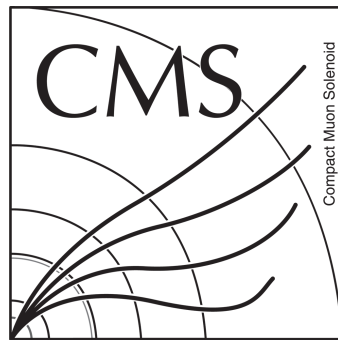


Figure 1.8: Higgs production Feynman diagrams for proton-proton collisions.

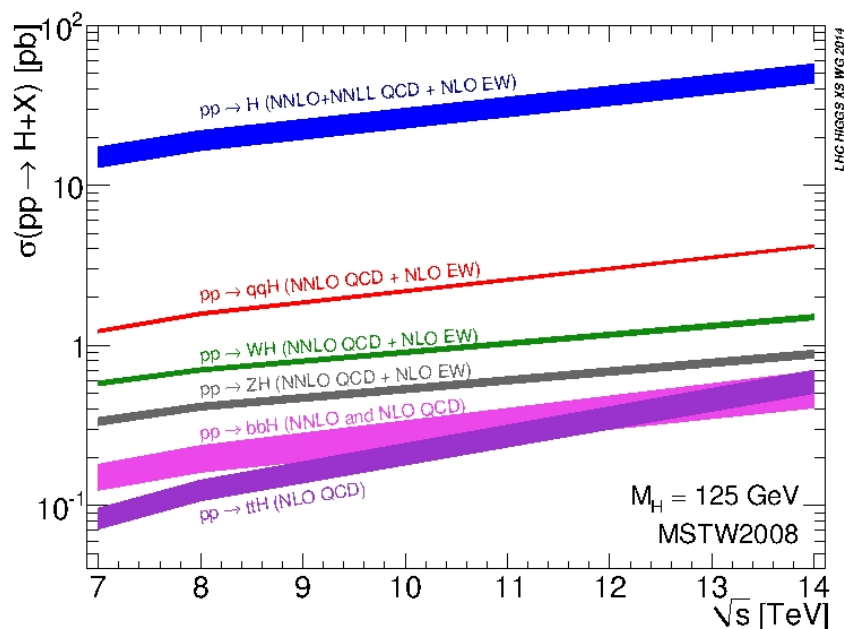


Figure 1.9: Higgs production cross section theoretical predictions as function of center of mass energy.

³¹⁴ 1.4.1 Decay channels

- ³¹⁵ Discussion of Higgs decays and relative importance also related to the resolution
³¹⁶ of channels.

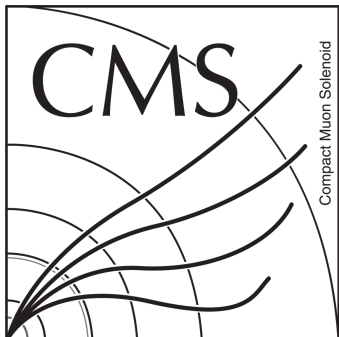


Figure 1.10: Feynman diagrams of Higgs decay: $b\bar{b}$ [left], diphoton [center] and golden channels [right]

³¹⁷ 1.4.2 Higgs properties

³¹⁸ Electric charge

- ³¹⁹ Higgs neutrality description.

³²⁰ Spin

- ³²¹ Importance of spin parity determination to know if it's the SM one.

³²² Mass and width

- ³²³ Mass and width measurements.

³²⁴ 1.5 Hierarchy problem and other limitations

- ³²⁵ The SM has been one of the most successful theories on the history of physics.
³²⁶ With only 19 free parameters, is able to make thousands of predictions that have
³²⁷ been measured and tested over the last seventy to eighty years. However some
³²⁸ aspects in the model are not completely understood. The most important one
³²⁹ is the so-called hierarchy mass problem. At tree level, the Englert-Brout-Higgs
³³⁰ boson has a mass $m_H^2 = -2\mu^2$, but the physical mass also contain the one-loop

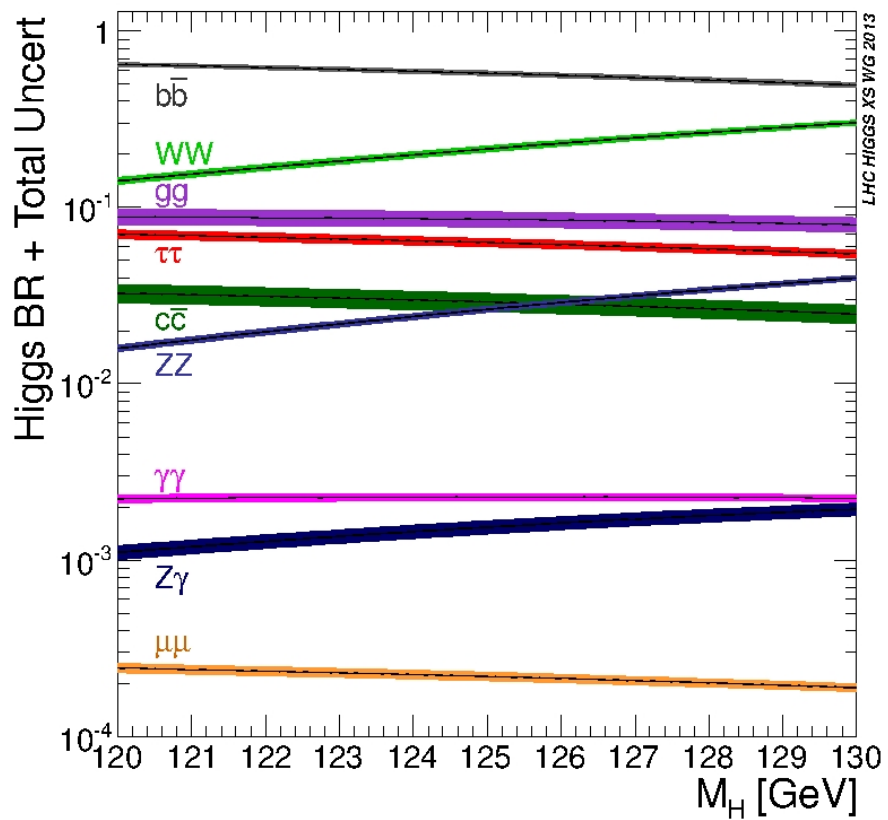


Figure 1.11: Higgs decay branching ratios.

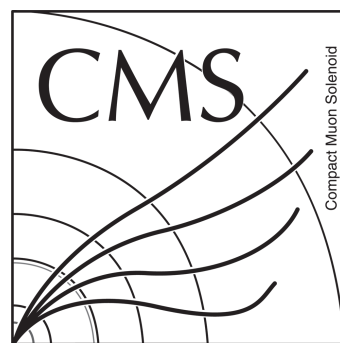


Figure 1.12: Higgs spin parity measurement

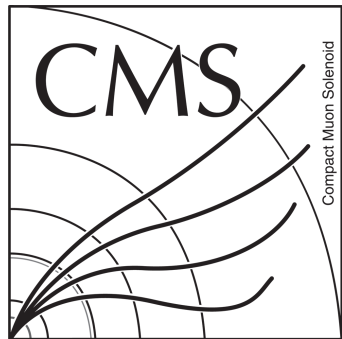


Figure 1.13: ATLAS and CMS combination of Higgs mass measurement [left] and signal strength for searches performed by CMS in different Higgs channels [right]



Figure 1.14: Higgs mass observation by CMS collaboration in the diphoton [left] and golden channels [right].

331 contributions from fermions that interact with it, as the top quark. The Feynman
332 diagram for such contribution can be seen in figure 1.15.

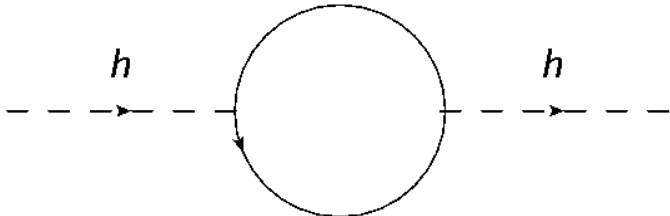


Figure 1.15: One loop diagram for contributions to the mass of the Englert-Brout-Higgs boson from interactions with fermions

333 Such contributions add up giving a mass greater than simple tree level mass.
334 Each fermion contributes proportionally to its mass, what means that the top
335 quark contributes the most. Moreover, if there are in nature heavier fermions that
336 also interact with the Englert-Brout-Higgs boson they will also contribute to its
337 mass. With such considerations one can expect the Englert-Brout-Higgs boson to
338 be much greater than 125 GeV, and in principle not even of the order of 100 GeV
339 but greater than 1 TeV. However the real relevance or significance of this problem
340 at theoretical level has been discussed extensively, for example at [9], the majority
341 of the community agrees there is something to be understood on the subject.

342 The most famous proposed solution to this problem is supersymmetry (SUSY) [10].
343 It proposes the existence of an additional symmetry between fermions and bosons,
344 at a given point of the history of universe nature didn't distinguish between
345 fermions and bosons. However, we know this does not happen at the present,
346 and then this symmetry should be broken. Such symmetry implies the existence
347 of a super-symmetric partner for each particle, a super-partner. A fermion for each
348 boson and vice versa. This SUSY procedure doubles the particle content of the
349 model where it's applied. Before breaking SUSY, a particle and it's partner have
350 the same mass. In this feature is where the hierarchy problem is solved. On figure
351 1.16 one can see the one loop diagrams for the mass of the Englert-Brout-Higgs
352 boson from the top and its super-partner the stop. Whereas, the top contribution
353 is positive, the stop contribution is negative but equal in value, then cancelling
354 between them.

355 But this solution works exactly only if SUSY is not broken. As we know SUSY
356 has to be broken, there has been developed in the literature different ways to break
357 SUSY and still offer a solution to the hierarchy problem, leading normally to solutions
358 that need a fine adjustment of the parameters of the theory. This represents
359 for some theoreticians a problem itself: Fine-tuning or Naturalness. Extensive

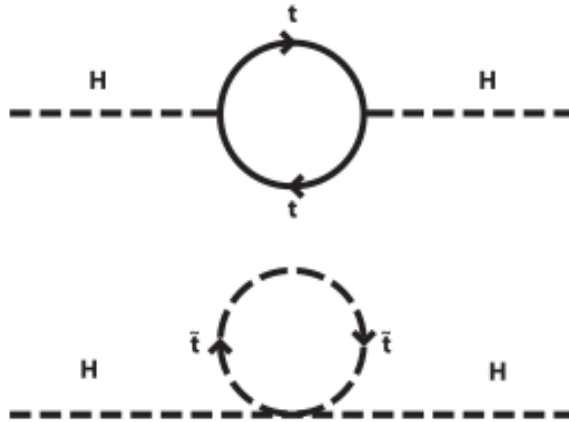


Figure 1.16: One loop diagrams for contributions to the mass of the Englert-Brout-Higgs boson from the top and the stop

360 searches for SUSY particles have been performed, accordingly to different model
 361 realizations MSSM [11, 12], CMSSM, etc.

362 While hierarchy problem is an internal problem of the SM, there are several
 363 questions that have not been solved. For example, how gravity is understood
 364 in the frame of QFT's, why there is only 3 generations of leptons and quarks,
 365 why there is only 4 fundamental forces among others. In addition, there have
 366 been experimental questionings to the SM. The mos important one is the masses
 367 of neutrinos. In the SM neutrinos are massless, careful measurements, [13, 14],
 368 have shown that neutrinos can oscillate between different flavors, phenomenon
 369 only possible if neutrinos have a mass. Measurements of solar and atmospheric
 370 neutrino oscillations have been the most important proof of physics beyond the
 371 SM.

372 From cosmological measurements, the Wilkinson Microwave Anisotropy Probe
 373 have shown that the universe is not only made by visible matter, but suggests that
 374 around 24% its made of dark matter. A type of matter not visible by means of
 375 light. It has also shown that 71% of the universe is composed of dark energy, what
 376 makes the universe to be in an accelerated state of expansion. These results can
 377 be seen in [15, 16]. Also the Planck probe has shown similar results, for example
 378 in [17]. The SM does not have any answer to this open problems so far.

379 Finally, there is known that the universe presents an asymmetry between mat-
 380 ter and antimatter, being the first much more abundant than the second. Such
 381 asymmetry can be obtained by CP-violating processes (C for charge and P for

382 parity). However the amount of CP violation present in the SM is not compatible
383 with the huge matter-antimatter asymmetry in nature. This problem, known as
384 baryon asymmetry, represent an additional huge challenge for particle physics.

385 In conclusion, the SM has been a formidable model that has helped us to under-
386 stand a huge amount of physics. It has done thousands of predictions that have
387 been measured and corroborated one by one in the last half-century. However,
388 this is not the end of the story, perhaps only the beginning. There are theoretical
389 and experimental motivations that lead us think that the SM is not the “final”
390 theory that could explain all subatomic phenomena in nature. Currently, there is
391 a mayor effort, both theoretical and experimentally, to understand and explain all
392 the remaining pieces. The present work is one of them.

393 In the next chapter, we present an extension of the SM that looks for a solution
394 to the discussed hierarchy problem.

³⁹⁵ 2 The CMS experiment at LHC

³⁹⁶ The CMS experiment is one of the biggest particle physics experiments on the
³⁹⁷ world. It is located at the ring of the LHC that is the main accelerator managed
³⁹⁸ by CERN, the European Organization for Nuclear Research or Centre Européenne
³⁹⁹ pour la Recherche Nucléaire by its french name. This center constitutes the biggest
⁴⁰⁰ center for research on particle physics all over the world. All along its 60 years of
⁴⁰¹ existence, from 1954, 21 member states have been joining it, but an overall of 113
⁴⁰² countries participate in different ways on this center.

⁴⁰³ On the present chapter we discuss in detail different aspects of the LHC acceler-
⁴⁰⁴ ator and the CMS experiment. In particular we make some emphasis in the CMS
⁴⁰⁵ sub-detectors related to jets, objects that play the main role on the search that is
⁴⁰⁶ the main subject of the present work. We also discuss the present state of both
⁴⁰⁷ machines, their achievements and the challenges that were overcome. Finally, also
⁴⁰⁸ the expectations and goals for the upcoming run II are mentioned.

⁴⁰⁹ 2.1 The Large Hadron Collider

⁴¹⁰ The Large Hadron Collider, or LHC [1], is a machine that accelerates and collides
⁴¹¹ protons and lead. This machine is the biggest particle collider nowadays with a
⁴¹² circumference of 27 km. It also achieves the highest energy by a collider up to
⁴¹³ present, planned to be 14 TeV at the center of mass of the collision. On the first
⁴¹⁴ run of the machine only 8 TeV were achieved, and next run is planned to start
⁴¹⁵ with 13 TeV. It's located in French-Swiss border near to Geneva. The tunnel for
⁴¹⁶ the machine was carved around 100 m under the ground, 45 m under the Jura
⁴¹⁷ mountains and 170 m under the Léman lake with an inclination of around 1.4%,
⁴¹⁸ sloping down towards the lake . This machine has used as much as possible old
⁴¹⁹ LEP buildings and sites, that was an electron-positron collider built between 1984
⁴²⁰ and 1989.

⁴²¹ The protons and heavy ions accelerated by the machine collide in different points
⁴²² where dedicated experiments are located to detect and study the product from the
⁴²³ collisions. The four main experiments located on the LHC ring are CMS [2, 3],
⁴²⁴ ATLAS [4], LHCb [5] and ALICE [6]. The first two are experiments of generic
⁴²⁵ purpose where searches for new physics and also precision measurements are per-
⁴²⁶ formed. LHCb is dedicated to the physics of the b-quark, and ALICE focuses on

427 the study of the quark-gluon plasma produced from heavy ions collisions. Even if
428 one of the principal objectives of the construction of the LHC was the search for
429 the Higgs boson, generic searches on new physics have been conducted from the
430 very beginning of the first data taking in 2009. Moreover, after the Higgs discov-
431 ery in 2012 there is a growing effort on the searches for new physics and precision
432 measurement of the properties of the Higgs.

433 The LHC is a complex machine composed of several parts. The two principal
434 parts are the injector chain and the main ring. A diagram of the whole CERN
435 complex can be seen in figure 2.1. The injector chain has different stages that
436 pre-accelerate protons and heavy ions to be injected into the main ring of LHC.

437 **2.1.1 Injector chain**

438 The injector chain begins with the proton source. Protons are extracted via ioniza-
439 tion of Hydrogen gas in the Duoplasmatron Proton Ion Source. Such extraction is
440 pulsed, what makes up the first bunch structure. The extracted protons are then
441 accelerated up to 50 MeV in the linear accelerator, Linac2, that dates from 1978.
442 After this first stage several steps are followed:

- 443 1. Linac2 injects proton bunches in the Proton Synchrotron Booster (PSB)
444 where they are accelerated to 1.4 GeV.
- 445 2. From PSB, the protons are delivered to the Proton Synchrotron (PS) where
446 they reach an energy of 25 GeV. In the PS the bunches are also split from 6
447 initial bunches to 72 spaced by 25 ns.
- 448 3. Finally, the pre-acceleration chain is finished by the SPS, Super Proton Syn-
449 chrotron. There the bunches are accelerated up to 450 GeV right before
450 being inserted into the main LHC ring.

451 The whole pre-acceleration chain has been optimized to obtain the best possible
452 performance on the final acceleration in the LHC main ring. All parameters are
453 carefully controlled, for example the number of bunches, the separation between
454 bunches, the separation between trains of bunches or the injection energy to each
455 subsystem. It's also remarkable to notice the level of control achieved in the
456 bunches manipulation, from old subsystems as the PS from 1959 or the newest,
457 the SPS that dates from 1976.

458 Some recent plans for future accelerator have been studied using the LHC main
459 ring as injector for a bigger accelerator, for example the so called FCC (Future Cir-
460 cular Collider) at CERN. The FCC could be built perform proton-proton, electron-
461 positron or electron-proton collisions, versions that are called respectively FCC-hh,
462 FCC-ee and FCC-he. The FCC-hh is being designed to achieve 100 TeV of center
463 of mass energy in a tunnel of 80-100 km of circumference.

CERN Accelerator Complex

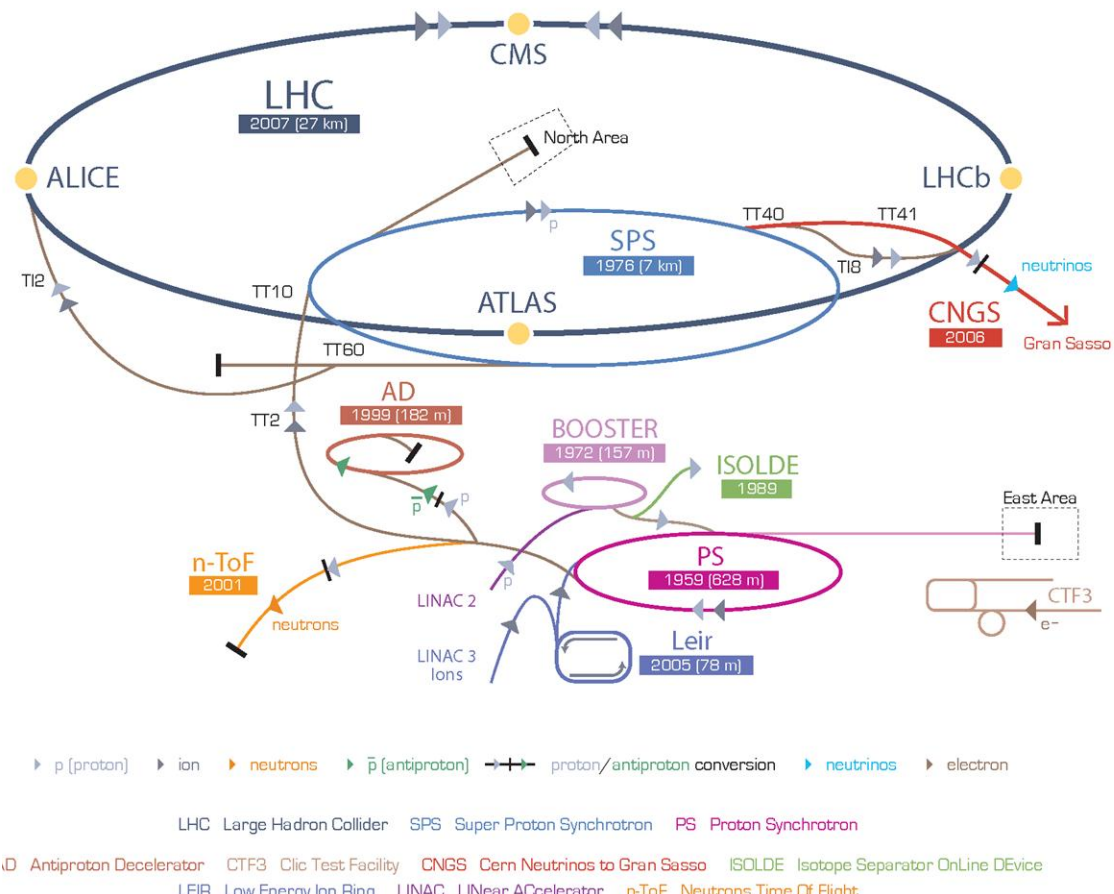


Figure 2.1: Organization of CERN accelerator complex

464 **2.1.2 Main ring**

465 The main ring is composed of two rings that accelerate the proton bunches in
466 opposite directions, clock-wise and counter clock-wise. An schematic view of the
467 design of the main ring can be seen in figure 2.2. The rings crosses in different
468 points in order to collide the protons and they are divided in eight straight sections
469 and eight arcs. In each octant bunches are controlled by dipole magnets. These
470 complex magnets, in figure 2.3, need to produce a very strong magnetic field in
471 order to be able to bend a 7 TeV beam of protons. This intense magnetic field, 8.33
472 T, in opposite directions, is produced by electrical currents that are only achievable
473 by means of superconductivity. All the 1232 dipoles operate at a temperature of
474 1.9 K, under cooling by liquid helium. They also operate under ultra-high-vacuum.
475 The beam lines with a pressure less than 10^{-9} mbar and the whole dipole system
476 with 10^{-6} mbar, that serves also as insulating system from the surroundings. In
477 addition, the LHC main ring has other magnets that focus and correct different
478 characteristics of the beam: 520 quadrupoles, 2464 sextupoles, 1232 octupoles.

479 **Luminosity**

480 In collider physics, such as the LHC, the figure of merit is the luminosity, given in
481 equation 2.1. The number of events per second is proportional to the luminosity,
482 hence is the quantity to be maximized by the design and operation of the acceler-
483 ator. The collider characteristics depend on the number of bunches in the ring n_b ,
484 the number of protons per bunch N_b , the revolution frequency f_{rev} , the relativistic
485 gamma factor γ , the normalized rms transverse beam emittance ϵ_n and the beta
486 function at the interaction point β^* . The denominator on 2.1 can also be rewritten
487 in terms of the horizontal and vertical width of the bunches at the crossing, σ_x^*
488 and σ_y^* . In addition, there is the geometric reduction factor (R) that introduces
489 a dependence on the crossing angle of the bunches at the interaction points. In
490 table 2.1.2 can be found the LHC beam parameters at injection and collision.

$$L = \frac{n_b N_b^2 f_{rev} \gamma}{4\pi \epsilon_n \beta^*} R = \frac{n_b N_b^2 f_{rev}}{4\pi \sigma_x^* \sigma_y^*} R \quad (2.1)$$

491 At the crossing points, the number of events coming from collisions and produced
492 via a specific process, is directly proportional to the luminosity provided by the
493 collider, as in equation 2.1.

$$N_{events} = L \sigma_{process} \quad (2.2)$$

494 where $\sigma_{process}$ is the cross section of the process.

495 The total cross section of a proton-proton collision from the crossing of two
496 bunches at 14 TeV is 100-110 mb [7], from three different scattering processes:

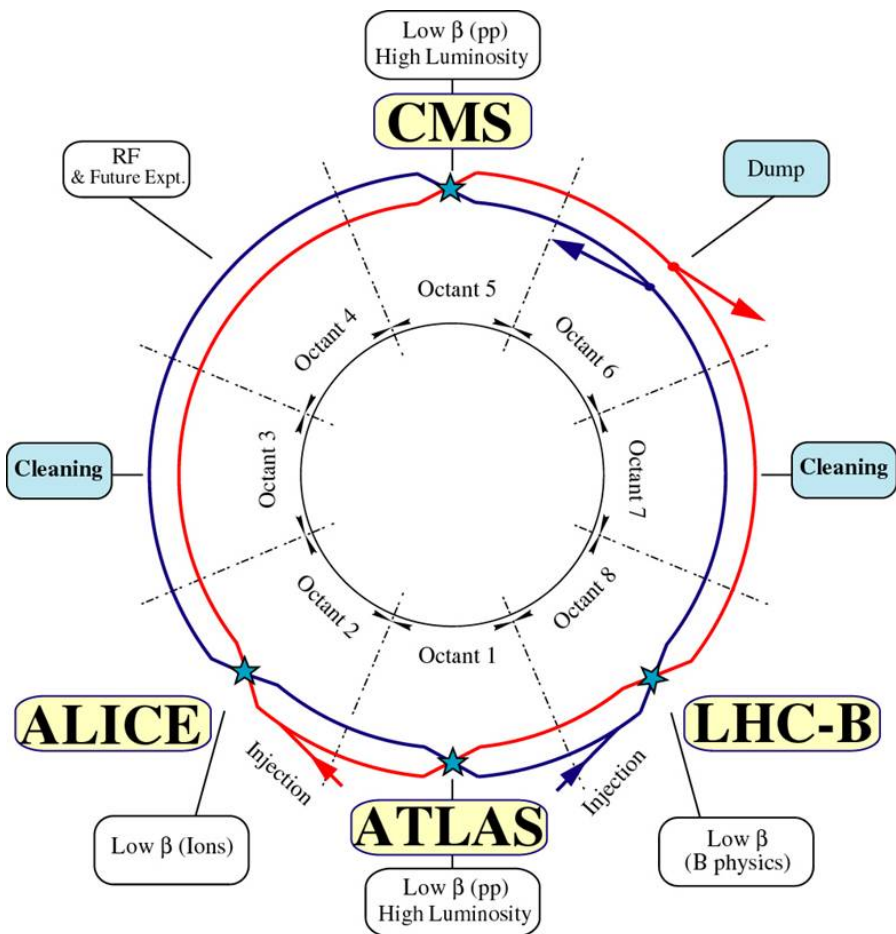


Figure 2.2: Schematic of the LHC main ring design.

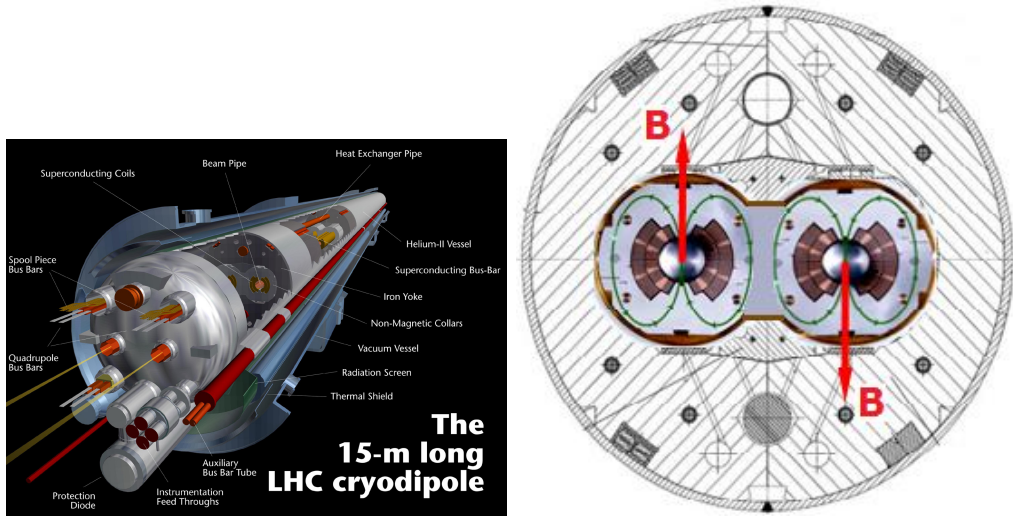


Figure 2.3: Design of LHC cryodipole and the magnetic field that bends the beam in the main ring.

497 elastic, diffractive and inelastic. In the elastic scattering the protons only ex-
 498 change momenta but their structure remain unchanged, that is the case for the
 499 majority of collisions. In diffractive scattering momenta is exchanged and also new
 500 particles are produced in addition to the two final protons. Finally, in inelastic
 501 scattering, the constituents of the protons, the partons, interchange a big amount
 502 of momentum and produce a large quantity of particles. The inelastic processes
 503 contribute less than diffraction to the total cross section. While inelastic collisions
 504 produce particles in the central rapidity (defined in 2.2.1) region, diffractive and
 505 elastic final products have a large rapidity. Only in the hard interactions, inelas-
 506 tic scattering, color is exchanged, being the reason to fill up the central rapidity

Parameter/units	Injection	Collision
Energy [GeV]	450	7000
Luminosity [$\text{cm}^{-2}\text{s}^{-1}$]		10^{34}
k_b Number of bunches		2808
Bunch spacing [ns]		24.95
N_b intensity per bunch [protons/bunch]		1.15×10^{11}
Beam current [A]		0.58
ϵ_n normalized rms transverse beam emittance [μm]	3.5	3.75
f_{rev} revolution frequency [kHz]		11.25

507 region.

508 From the crossing of two bunches not only one proton-proton interaction is
509 expected. In average, 25 interactions are expected for each crossing. From them,
510 only one is coming from an inelastic collision, that is the type of process of more
511 interest for detectors as CMS or ATLAS. This fact puts an additional difficulty
512 to the detectors in order to extract the hard interaction from all the elastic and
513 diffractive collisions happening at same time. Such phenomena is known as Pile-
514 Up, an illustration of a collision with high pile-up can be found on figure 2.4 as
515 seen by the CMS detector.

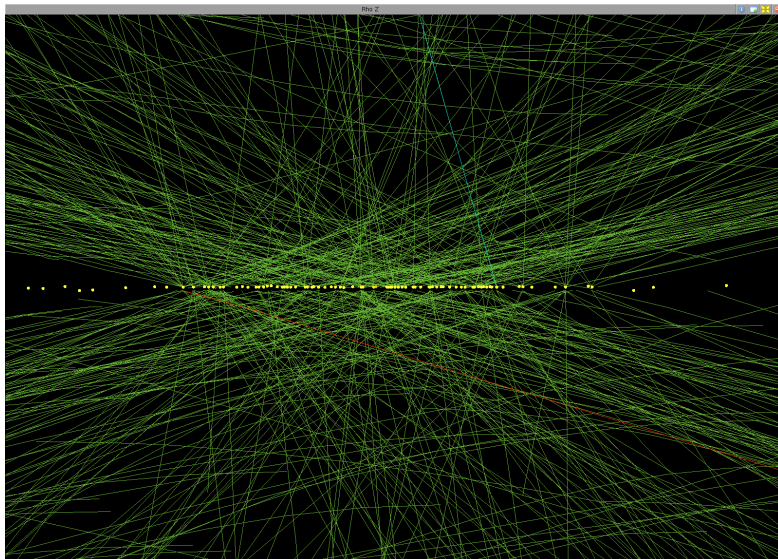


Figure 2.4: High pile-up event (78 interactions) seen by CMS detector. Event 35655522, from 198609 run, lumi 56, recorded on 2012. Image credit: Andre Holzner ©CERN

516 2.1.3 Run 1

517 On February 10 of 2013 the first stable run of the LHC reached an end. This run,
518 now called Run 1, started on November 20 of 2009. LHC was originally planned
519 to start in 2008, but an incident on one of the electric connections of one of the
520 magnets forced to stop on the 19th of September of the same year. From the
521 restart in 2009, the energy was augmented from 450 GeV to 4 TeV per beam. The
522 23th of September 2009 the first collisions were detected by the experiments. One
523 week after, the achieved center of mass energy was $\sqrt{s} = 2.36$ TeV, already higher
524 than Tevatron (0.98 TeV).

525 In 2010, from 30th March to 6th December 3.5 TeV per beam were reached de-
 526 livering near 50 pb^{-1} . With the same energy, approximately 6 fb^{-1} were delivered
 527 in 2011.

528 In 2012, the center of mass energy reached one additional TeV, $\sqrt{s} = 8 \text{ TeV}$,
 529 and around 20 fb^{-1} of integrated luminosity were delivered between April and
 530 December. On figure 2.5 can be seen the progress of the recorded luminosity by
 531 CMS for 2010-2012 period. The first six weeks of 2013 were devoted to proton-lead
 532 collisions.

533 After this very successful run, the LHC has been stopped for more than a year
 534 for repair and maintenance of different systems in the experiments and in the LHC
 535 itself to achieve higher energies. After this period, known as Long Shutdown or
 536 LS1, the LHC is planned to restart a new run on the early spring of 2015.

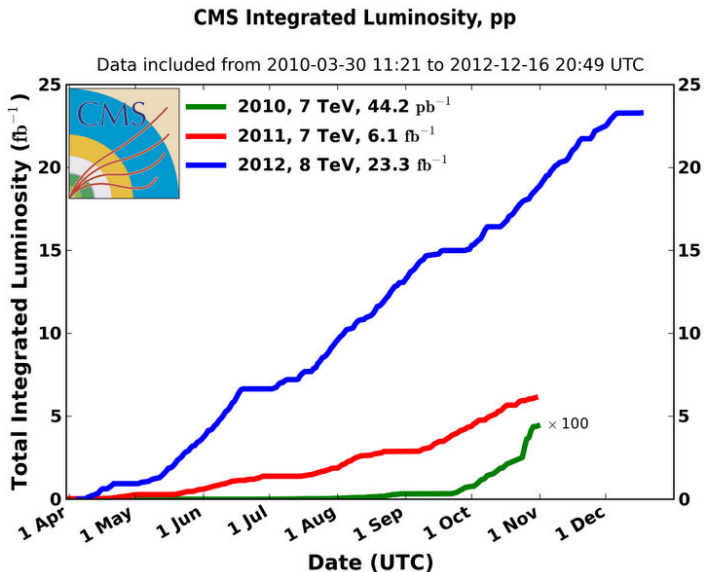


Figure 2.5: CMS integrated luminosity for proton-proton collisions delivered by LHC. ©CERN

537 2.1.4 Other experiments at LHC

538 On the main ring there are several experiments depending on the collisions de-
 539 livered by the LHC main ring. The biggest are CMS [2] and ATLAS [4], both
 540 of them generalist experiments designed to do precision measurements as well as
 541 new physics searches. Mainly recording proton-proton collisions, they have also

542 recorded lead-lead and proton-lead collisions during the run 1. Both of them were
543 designed for high instantaneous luminosity, $L = 10^{34} \text{cm}^2\text{s}^{-1}$.

544 In addition, there are two other experiments designed for specific purposes. The
545 LHCb [5] that focus on the study of the physics of the b-hadrons, specially related
546 to the CP violation, and ALICE [6] built for the study of strongly interacting matter.
547 The first of them record proton-proton collisions at an instantaneous luminosity
548 of $10^{32} \text{cm}^2\text{s}^{-1}$ and the second record ion-ion collision with $L = 10^{27} \text{cm}^2\text{s}^{-1}$.

549 The CMS experiment is going to be described in detail in section 2.2. In the
550 following sections we are going to present very briefly the other three experiments
551 mentioned above.

552 ATLAS

553 The ATLAS experiment (A Toroidal LHC ApparatuS) is the biggest LHC experiment.
554 It's located at point one, as displayed on figure 2.2, on the LHC main ring.
555 It's a cylindrical detector similar to CMS, about 45 meter long, 25 meter high, and
556 weights around 7000 tons. ATLAS main components are, from inside to outside, a
557 tracking system, an electromagnetic calorimeter, a hadron calorimeter and muon
558 chambers. In between these subsystems there is an internal solenoidal magnet and
559 a set of external toroidal magnets. The detector design is presented on figure 2.6.

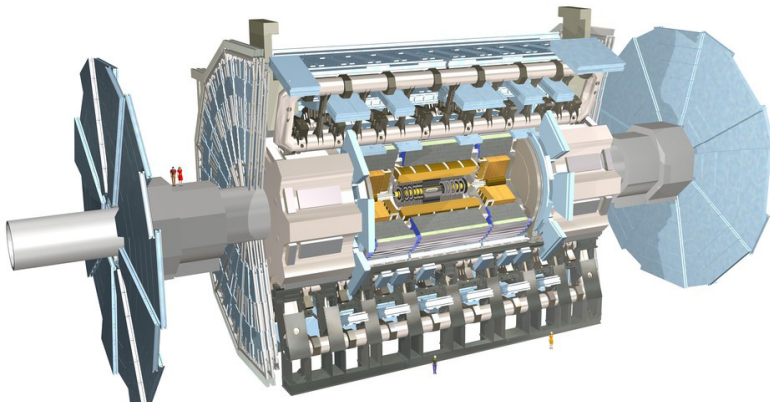


Figure 2.6: ATLAS detector internal view. ©CERN

560 On the human resources side, ATLAS experiment configures a collaboration
561 of around 3000 persons, coming from 117 universities around the world, from 38
562 countries. Thirty percent of the collaboration are students.

563 **LHCb**

564 LHCb detector, hosted at point 8 of the LHC main ring, has a different design than
565 CMS and ATLAS. Smaller than these, its design mainly focus to be able to detect
566 particles produced close to the beam direction. This is the reason why it is not
567 cylindrically but conically shaped, in two detection arms 2.7. It also has the same
568 main parts, a tracking system with a very precise vertex locator, electromagnetic
569 and hadron calorimeters, muon chambers and magnets. Its major specificity is
570 a system that allows to identify different hadrons, the RICH detectors, a crucial
571 feature for the study of strong interacting matter. It measures 21 m long, 10 m
572 high and 13 m wide, and weights 4500 tons. A view of the detector can be found on
573 figure 2.7. The LHCb collaboration groups around 700 persons from 50 different
574 universities over 15 countries.

575 **ALICE**

576 The ALICE experiment (A Large Ion Collider Experiment) is located at point 2
577 of the LHC main ring, measures 16 m high, 16 m wide and 26 m long, and weights
578 10000 tons. Designed for heavy ion physics, it is able to detect an extremely high
579 number of tracks per event. Its main subsystem is the Time Projection Chamber
580 (TPC), a 90 m³ gas chamber filled with a mixture of Ne, CO₂ and N₂ operated in
581 a solenoid of 0.5 T. It allows to measure leptonic and hadronic charged particles in
582 a momentum range from 0.5 to 10 GeV/c. The experiment structure can be seen
583 on figure 2.8. ALICE collaboration counts around 1500 people, from 154 physics
584 institutes in 37 countries.

585 **2.2 The Compact Muon Solenoid (CMS)**
586 **experiment**

587 The CMS detector, hosted at point 5 of the LHC main ring (see figure 2.2), is the
588 second biggest LHC experiment. Cylindrically shaped, measures 15 m of diameter
589 and 28.7 m long, and weights 14000, making it the heaviest LHC experiment. Its
590 subsystems are concentrically located from the collision point in the beam line. It's
591 called compact because the whole calorimetry is inside the solenoid magnet, and
592 muon solenoid because it has a very precise muon detection. Its main characteristic
593 is the strong 3.8 T solenoid magnet. A representation of the detector can be found
594 in figure 2.9. The CMS collaboration is formed by around 2600 scientists, of which
595 900 are students, from 181 institutes over 41 countries.

596 CMS has been designed to be able to do very precise identification of parti-
597 cles originated from the collisions and their properties. For the measurement of

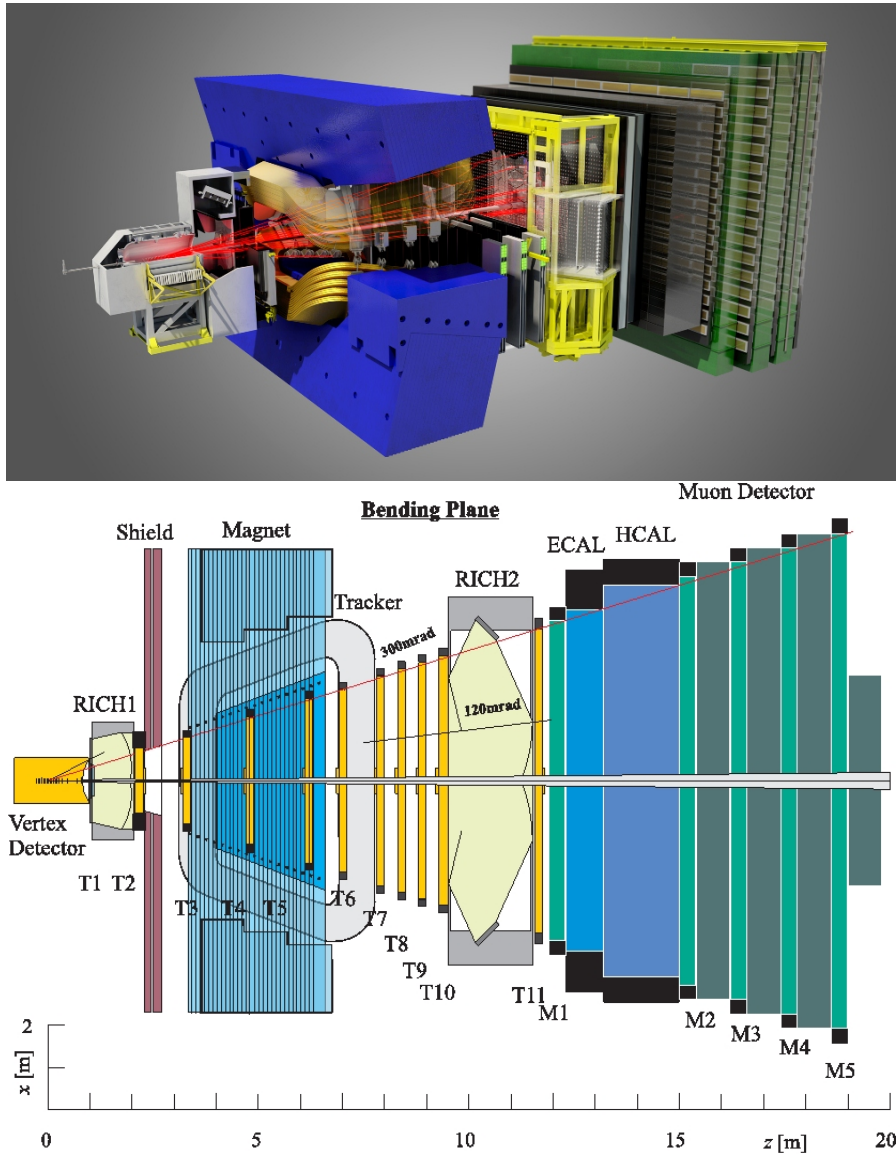


Figure 2.7: LHCb detector internal view [top] and view from the top [bottom].
©CERN

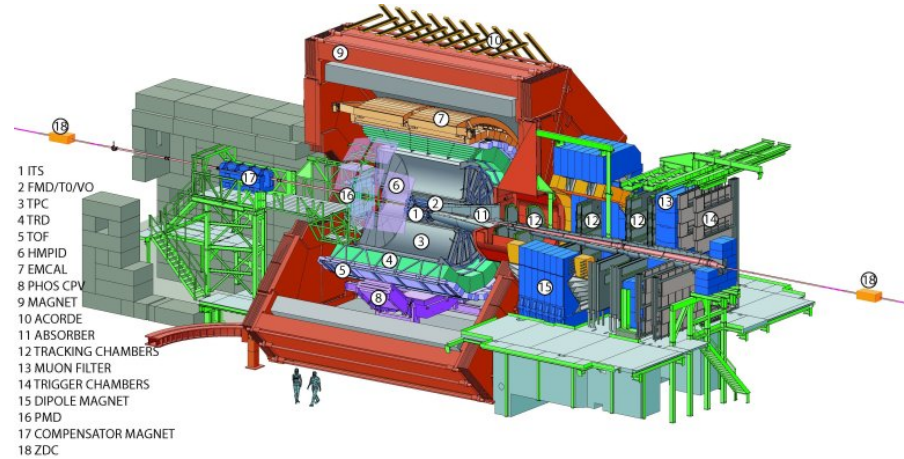


Figure 2.8: ALICE detector internal view. ©CERN

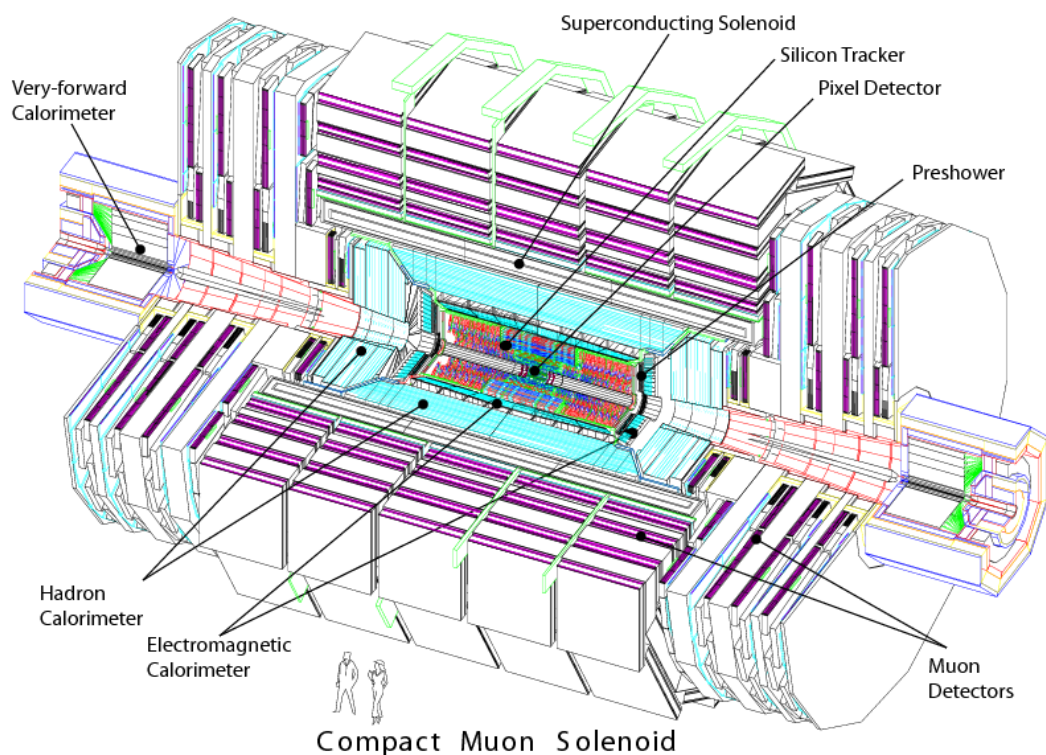


Figure 2.9: CMS detector internal view. ©CERN

598 the momentum of the charged particles, CMS counts with a very strong magnet
 599 that allows to bend very energetic particles. In addition, the calorimeters allow to
 600 measure accurately the energy from hadrons, electrons and photons. At the most
 601 external layer, the muons chambers measuring muons properties, and in the in-
 602 nermost the tracking system that reconstructs the collision points and the charged
 603 particles tracks. In figure 2.10 can be found a representation of the different sub-
 604 systems of CMS and how particles are reconstructed from them.

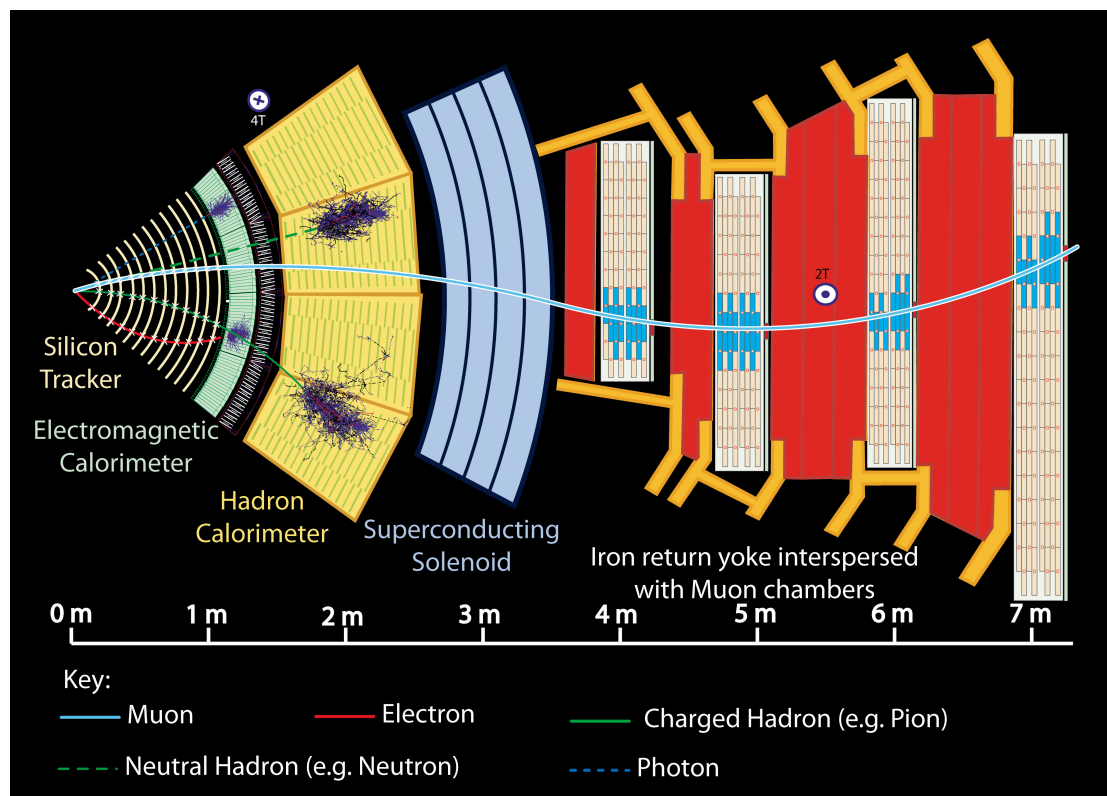


Figure 2.10: CMS sub-detectors and particle identification. ©CERN

605 2.2.1 Coordinate system

606 The origin of coordinates defined on the CMS detector is located on the nominal
 607 collision point, the “interaction point”. From there, the z-axis is defined along the
 608 beam pipe line pointing towards the Jura mountains. The positive/negative z-axis
 609 directions define the positive/negative sides of the detector. The y-axis is defined
 610 towards the zenith and the x-axis towards the center of the LHC ring. Due to the

611 inclination of the LHC plane, this coordinate system is slightly tilted with respect
 612 to the true vertical. A representation of the coordinate system definition can be
 613 found in figure 2.11.

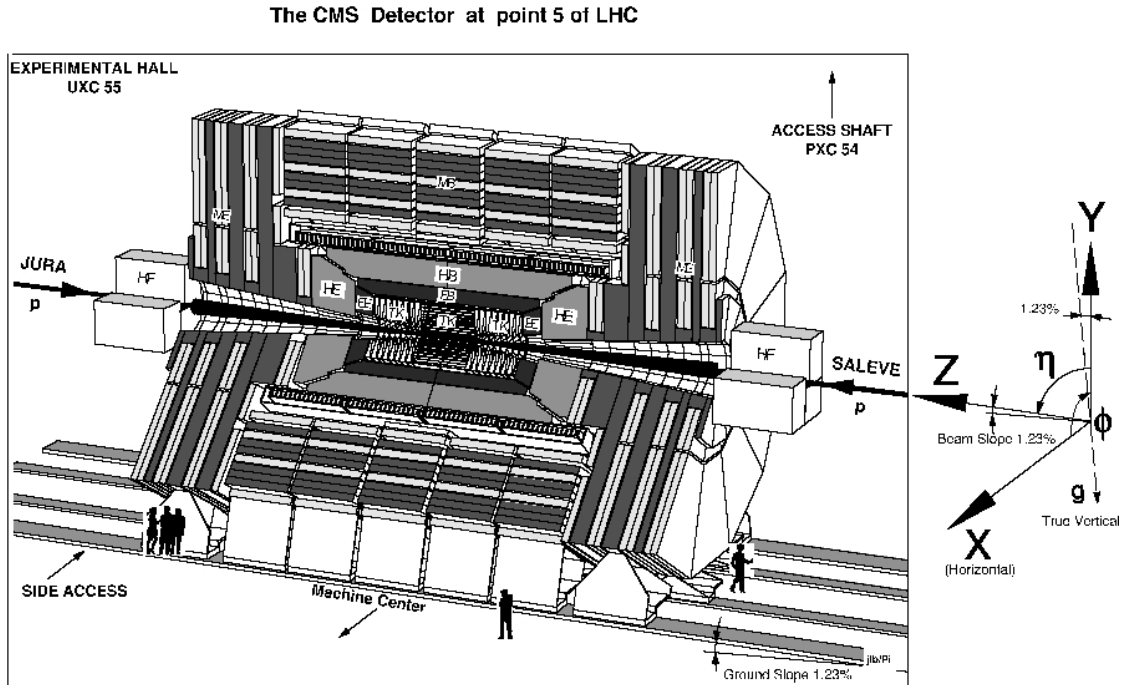


Figure 2.11: CMS coordinate system. ©CERN

614 We can also define two angles: the ϕ angle in the x-y plane from the x-axis
 615 towards the positive y-axis, and the θ angle in the z-y plane from z-axis towards
 616 the positive y-axis. In experimental particle physics is preferred to work with
 617 relativistic invariant quantities, reason why instead of working with θ we define
 618 the pseudorapidity η , equation 2.3.

$$\eta = -\ln \left(\tan \left(\frac{\theta}{2} \right) \right) \quad (2.3)$$

619 One can define another relativistic invariant quantity, the rapidity y as from
 620 equation 2.4. With \mathbf{p} being the momentum vector and E the energy of a given
 621 particle, p_L denotes its longitudinal component, that in our case is the same z-
 622 component.

$$y = \frac{1}{2} \ln \left(\frac{E + p_L}{E - p_L} \right) \quad (2.4)$$

623 On the limit that the mass of the particle is very small compared to its momentum,
 624 one can replace approximate the particle energy by the momentum magnitude,
 625 giving rise to the definition of the pseudorapidity in terms of the momentum of
 626 the particle $\eta = \frac{1}{2} \ln \left(\frac{p+p_L}{p-p_L} \right)$

627 We define also the radial coordinate over the x-y plane, plane that is called
 628 the transverse plane being orthogonal to the longitudinal direction, the z-axis. In
 629 such plane are also defined the transverse quantities of particles, as the transverse
 630 momentum p_T . Finally, for any two objects an angular distance can be defined in
 631 the $\eta - \phi$ plane, as in equation 2.5.

$$\Delta R = \sqrt{(\Delta\eta)^2 + (\Delta\phi)^2} \quad (2.5)$$

632 2.2.2 Magnet

633 In order to measure the momentum of the charged particles going inside the de-
 634 tector is crucial to apply the correct magnet field, sufficiently strong to bend very
 635 energetic particles. The momentum of a charged particle inside an uniform mag-
 636 netic field can be written as

$$p = \gamma mv = qBr \quad (2.6)$$

637 where B is the magnitude of the magnetic field, γ the usual relativistic factor, m
 638 the mass of the particle, v its rapidity, q its charge and r the bending radius. The
 639 sagitta of the arc is

$$s = \frac{L^2}{8r} = \frac{qBL^2}{8p} \quad (2.7)$$

640 with L the trajectory length that the particle moved inside the magnetic field.
 641 Inside a solenoid L is equal to the radius of it.

642 From relation 2.7 it is possible to deduce that the resolution on the momentum
 643 of the particle has an inverse dependence with the magnetic field and the radius
 644 of the solenoid, as shown in equation 2.8. From there, for a better resolution it is
 645 needed to increase the magnetic field and the radius of the solenoid.

$$\frac{dp}{p} \propto \frac{p}{BL^2} \quad (2.8)$$

646 The design of CMS magnet target both features, it utilizes a large solenoid of 6
 647 m of diameter and 13 m long. It's made of 4 layers of windings of NbTi cable that
 648 is cooled to 4.45 K in order to achieve the superconducting state. This magnet is
 649 able to produce an uniform magnetic field inside of it of 3.8 T. Outside the magnet
 650 5 wheels and 3 disks of iron are placed in order to return the flux of the magnetic

651 field, inducing just a 2 T radial magnetic field outside the solenoid. This iron yoke
652 is the main contribution to the detector weight, 10000 tons. The muon chambers
653 are located in between the iron yoke.

654 **2.2.3 Tracker system**

655 The tracker system has been designed to specifically address the reconstruction
656 of high p_T leptons, with particular interest in the isolation of electrons and, as a
657 consequence, to isolate photons. Also the tracker fulfill granularity requirements
658 to reconstruct secondary vertexes to tag and reconstruct B-hadrons. The tracker
659 system is able to reconstruct tracks of particles with at least 2 GeV of p_T with
660 $|\eta| < 2.5$. Charged hadrons are reconstructed with an efficiency of at least 85%
661 for $p_T = 1$ GeV and up to 95% for p_T above 10 GeV. Another important point
662 that was taken into account is the fact that the tracker is the part of CMS most
663 exposed to radiation as it is the closest subsystem to the interaction point. The
664 tracker system was built highly resistant to radiation damage and is expected to
665 last for around 10 years. The pixel detector only lasts 2 years and was replaces
666 during LS1.

667 The tracker has been built with two different technologies: Pixels and Silicon
668 Strips. They are arranged concentrically in cylindrical volumes being the pixel
669 detector the innermost. The CMS tracker extends to a radius of 1.1 m and a
670 around 2.7 m on each z direction, reaching a coverage in $|\eta|$ between 0 and 2.5.
671 The pixel system is in the region with a radius below ≈ 20 cm and the silicon
672 detector surrounding the pixel system.

673 The pixel system is formed by three barrel layers ($r = 4.3$ cm, $r = 7.3$ cm and
674 $r = 10.4$ cm) and four end cap disks ($z = \pm 35.5$ cm and $z = \pm 46.5$ cm). It has
675 an approximate active surface of one square meter with approximately 70×10^6
676 pixels with a cell size of 100 μm by 150 μm . This pixel system allows to obtain
677 three highly precise points that are mainly used for reconstructing vertexes. Its
678 resolution in $r - \phi$ is shown in figure 2.12. In the same figure is shown the efficiency
679 to find hits per each barrel layer and end cap disk.

680 The Silicon Strip system is formed by an inner ($20 \text{ cm} < r < 55 \text{ cm}$) and outer
681 tracker ($55 \text{ cm} < r < 116 \text{ cm}$). The inner tracker is composed of a 4-layer barrel
682 (TIB for Tracker Inner Barrel) and 3 disks (TID for Tracker Inner Disks) in each
683 end cap. The outer tracker systems is composed of 6 layers in the barrel (TOB for
684 Tracker Outer Barrel) and 9 disks in each end cap (TEC for Tracker EndCap).

685 In figure 2.13, can be seen the disposition of all the tracker subsystems. From
686 the design of the tracker system the best resolution on the p_T measurement is
687 achieved in the $|\eta| < 1.6$ region, this due to the presence of more layers of detector
688 in the different subsystems, as shown in figure 2.14.

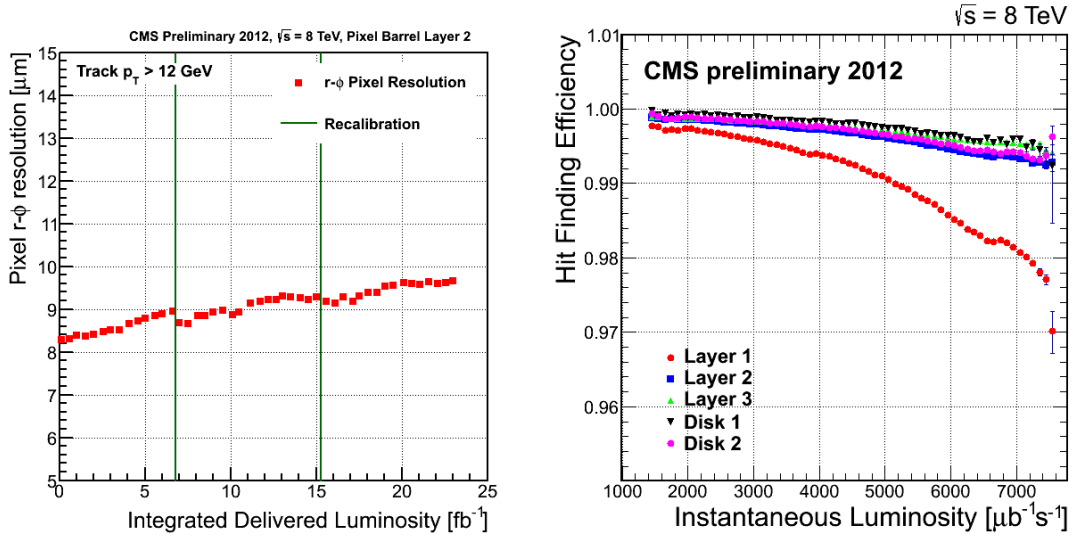


Figure 2.12: Resolution of the pixel detector in $r - \phi$ as function of the luminosity delivered to CMS detector [left] and efficiency of finding hits by the same detector [right].

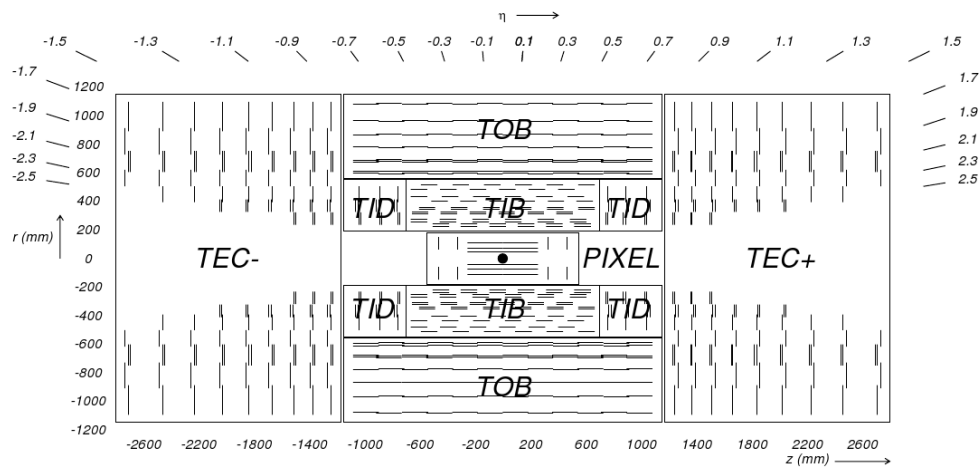


Figure 2.13: CMS tracker system configuration. ©CERN

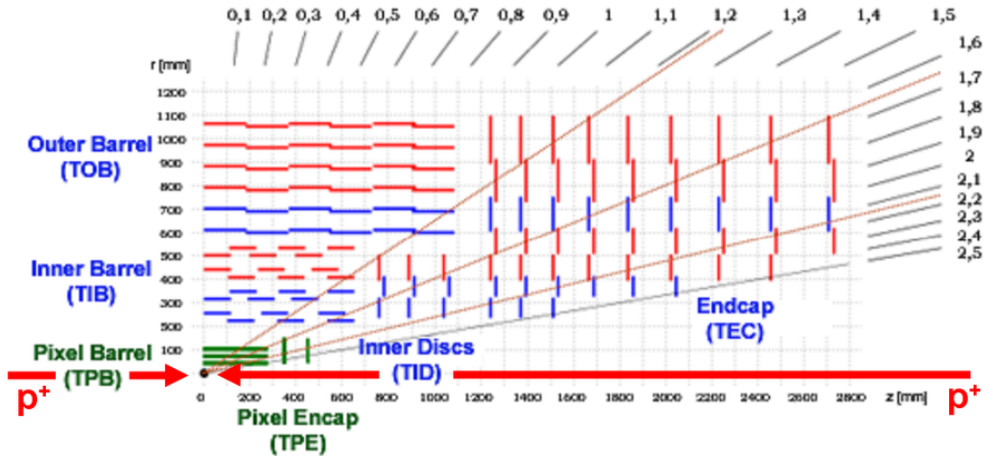


Figure 2.14: Tracker resolution with η . ©CERN

689 2.2.4 Electromagnetic calorimeter

690 The CMS ECAL (Electromagnetic CALorimeter) is the detector subsystem de-
 691 signed to stop photons and electrons to measure their energy. It's an hermetic
 692 cylindrical calorimeter made of 61200 crystals in the barrel ($|\eta| < 1.479$) and 7324
 693 in each end cap ($1.48 < |\eta| < 3$). The crystals material is lead-tungstate that
 694 is transparent, very dense (8.28 g/cm^3), has a small Moliere radius (2.2 cm) and
 695 a short radiation depth ($X_0 = 0.89 \text{ cm}$). This material has been chosen for the
 696 characteristics already described, but also because of its fast emitting scintillation
 697 light (about 25 ns) and its good energy resolution. The main disadvantage of this
 698 material is its high dependent response to the temperature (about 2% /°C), mak-
 699 ing crucial to maintain a stable temperature in the ECAL system. The crystals are
 700 distributed in 36 super-modules, 1700 crystals each, in the barrel (EB for ECAL
 701 Barrel) and in four 'Dee's, of 3662 crystals each, in the end caps (EE for ECAL
 702 End cap). In the EB the scintillation light is collected by Avalanche Photo-Diodes,
 703 or APD, and by Vacuum Photo-Triodes, or VPT, in the EE. A preshower system is
 704 installed in face of each end cap to allow a better discrimination between photons
 705 and π^0 's. A representation of the CMS ECAL can be found on figure 2.15.

706 The ECAL system requires constant correction to the lost of transparency due
 707 to aging by radiation. To correct the crystals performance the peak of the Z from
 708 di-electron events is used. In figure 2.16 can be seen the relative response of the
 709 crystals during LHC run I and the di-electron mass from electrons measured in the
 710 ECAL barrel. The aging of the crystals is controlled by a laser monitoring system
 711 that measures the transparency of the crystals. To test the corrections derived

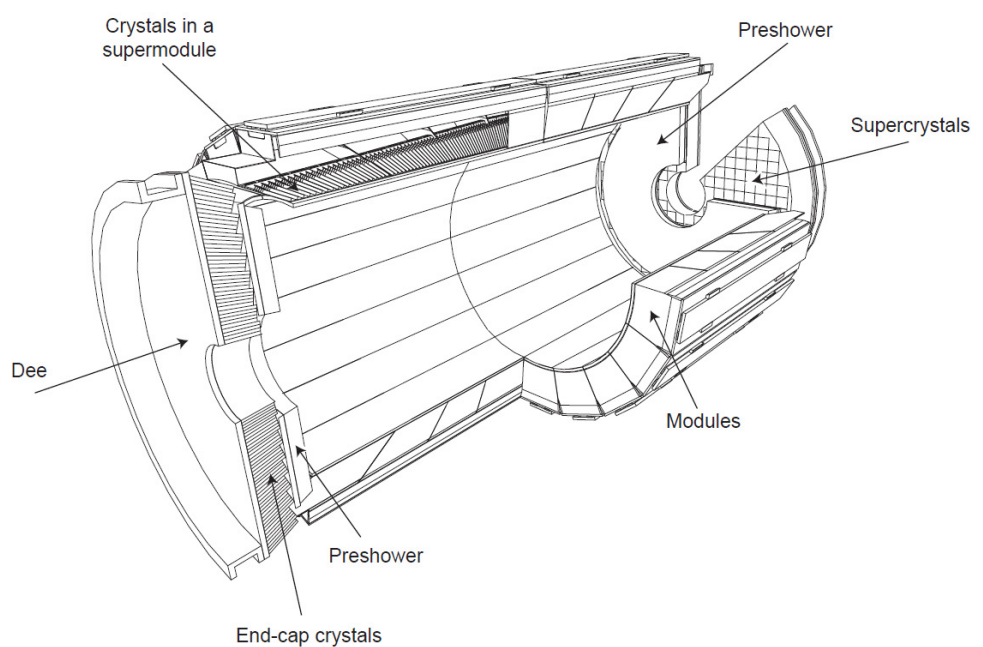


Figure 2.15: CMS ECAL representation. ©CERN

712 from the laser monitoring a comparison is performed between the reconstruction
 713 of electrons by the tracker and the ECAL. Such comparison in function of time
 714 can be seen in figure 2.17.

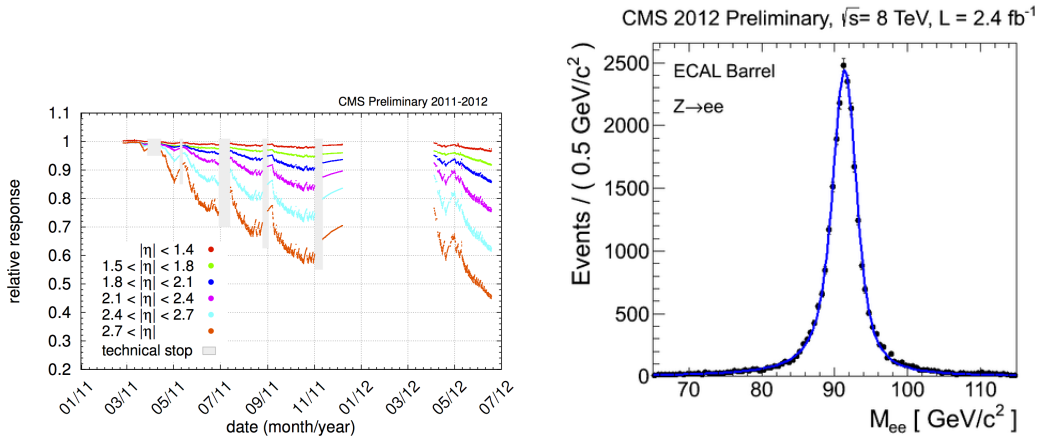


Figure 2.16: Relative response of the ECAL crystals as function of time, for different η regions [left]. Di-electron system mass from electrons identified in the ECAL barrel [right].

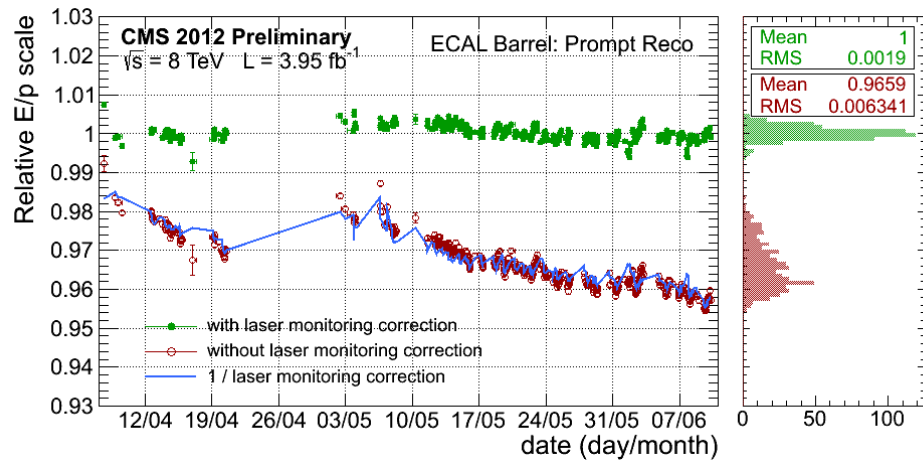


Figure 2.17: Relative E/p for electrons with and without laser monitoring as function of time. The electron energy E is measured by the ECAL while its momentum p is measured using the tracker information.

715 2.2.5 Hadronic Calorimeter

716 The CMS HCAL, for Hadronic CALorimeter, is the subdetector designed to mea-
717 sure the energy of hadrons produced in the collisions, mainly the neutral hadrons
718 because the charged hadrons are already traced by the tracker. It's also designed
719 to measure the missing energy coming from particles not being detected by any
720 of the subsystems, as neutrinos. It's an hermetic set of subsystems covering up to
721 $|\eta| < 5.2$:

- 722 • Hadron Barrel Calorimeter (HB): Covering $|\eta| < 1.4$ is located between the
723 ECAL barrel and the magnet.
- 724 • Hadron Endcap Calorimeter (HE): Extends the coverage of the barrel on the
725 region $1.4 < |\eta| < 3$.
- 726 • Hadron Outer Calorimeter (HO): Located outside the magnet, uses it as an
727 additional absorber.
- 728 • Hadron Forward Calorimeter (HF): Completes the coverage of the system
729 from $|\eta| = 3$ up to $|\eta| = 5.2$.

730 The CMS HCAL layout is shown in figure 2.18. The system is made of two
731 parts, an absorber to develop the hadronic showers and a scintillator to measure
732 the particles energy. The length scale of hadronic calorimetry is defined as the
733 interaction length corresponding to the mean free path of an hadron in a material.
734 The HB absorber is made of 40 mm thick steel plate, eight layers of brass plates of
735 50.5 mm thick, six brass plates of 56.5 mm thick and a steel plate of 75 mm thick.
736 The HE uses the same absorber but with thicker plates, of 79 mm. Between the
737 absorber plates a plastic scintillator, Kuraray SCSN81, 3.7 mm thick, is placed.
738 In the region with $|\eta| < 1.6$ the achieved granularity is $\Delta\eta \times \Delta\phi = 0.087 \times 0.087$
739 and $\Delta\eta \times \Delta\phi = 0.17 \times 0.17$ in the region with $|\eta| > 1.6$. This design gives a total
740 of 70000 tiles. The produced light in the HB is collected by optical fibers and
741 transferred to the Hybrid Photo Diodes (HPDs). This diodes were chosen thanks
742 to their small sensitivity to the magnetic field, an important feature because HCAL
743 is inside the solenoid magnet.

744 The HF design is very different from the rest of the HCAL subsystems. The
745 most important challenge for the HF is the high resistance to radiation, while in
746 the central rapidity region 100 GeV are deposited in average in the forward region
747 is 760 GeV. For this reason it was chosen a Cherenkov detector made of quartz
748 fibers with a steel absorber. The light produced in the HF is collected by photo
749 multipliers.

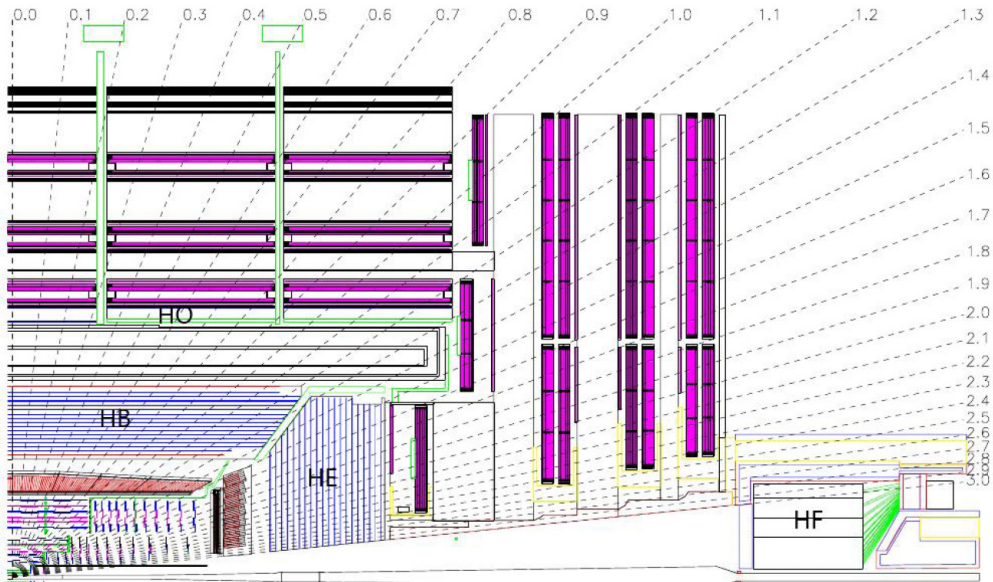


Figure 2.18: CMS HCAL representation. ©CERN

750 2.2.6 Muon chambers

751 The muon system of CMS is located at the most exterior layer of the detector due to
 752 the penetration power of this particle. Muons are not stopped by the calorimeters
 753 and, with neutrinos, they are able to escape the detector. The muon chambers
 754 are placed in a cylinder around the HO and in disks on the end caps. Three main
 755 characteristics have been fulfilled from the design: efficient muon identification,
 756 precision measurement of muon charge and momentum and fast measurement
 757 to provide trigger capabilities. The moun chambers are made of three different
 758 subsystems:

- 759 • Drift Tubes Chambers (DT): Located in the region with $|\eta| < 1.2$ and dis-
 760 posed in four layers. They consist of individual drift tubes of $50 \mu\text{m}$ of
 761 diameter anode wire with two electrode plates creating a drift electric field.
 762 The wall of the cell act as cathode. The cells are filled with a gas mixture,
 763 85% Argon and 15% CO_2 . The tubes are organized in plaques that are also
 764 organized in SuperLayers (SL) each one made of 4 plaques. The barrel is
 765 made of 250 DT's disposed in four cylinders separated by iron yokes.
- 766 • Cathode Strip Chambers (CSC): Installed in the end caps, provide a coverage
 767 up to $|\eta| = 2.4$ from $|\eta| = 0.9$. These chambers are multi-wire proportional
 768 chambers made of six planes of anode wires with 7 cathode planes. Four

769 CSC stations are placed in each end cap. The wires are oriented in azimuthal
 770 direction while the cathode planes are radially oriented, allowing a complete
 771 measurement of the position of the particle. This system is able to measure
 772 with a precision between the $75 \mu\text{m}$ and $150 \mu\text{m}$.

- 773 • Resistive Plate Chambers (RPC): This subsystem is made of gaseous parallel
 774 plate detectors. This detector is specially useful for triggering as it is very
 775 fast and have a good position resolution. There are 480 RPC distributed in
 776 6 layers in the barrel with the DT and in 3 layers in the end caps with the
 777 CSC, and covers the region with $|\eta| < 1.6$.

778 On figure 2.19 can be found a representation of the muon system with the
 779 different components. The DT and CSC system cover $|\eta| < 2.4$ without any gap.

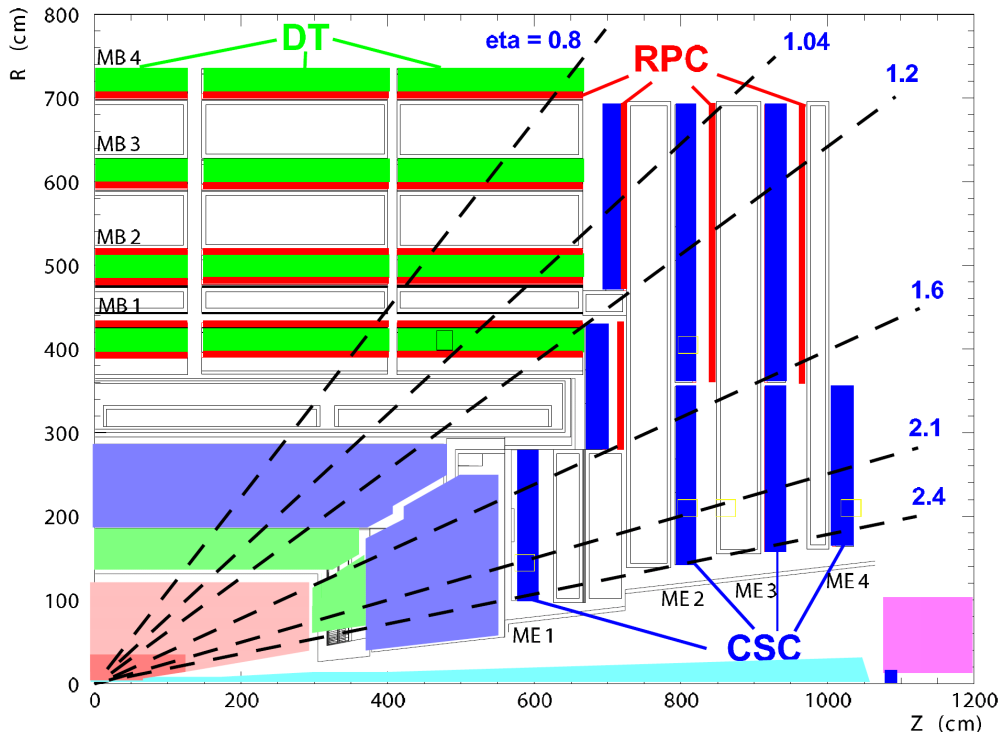


Figure 2.19: CMS muon chambers representation. ©CERN

780 The RPC subsystem efficiency depends on the voltage used and in the pressure
 781 of the injected gas. The efficiency on the RPC barrel during the run I data taking
 782 can be seen in figure 2.20.

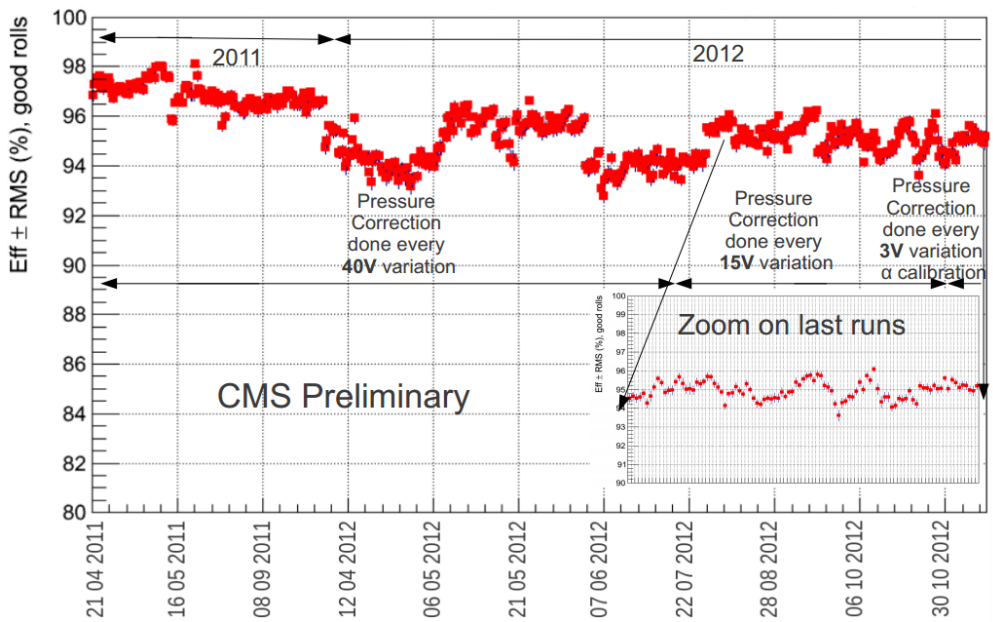


Figure 2.20: RPC Barrel efficiency during two years of data taking

⁷⁸³ 2.2.7 Trigger

⁷⁸⁴ LHC has been designed to collect data from proton-proton collisions every 25 ns,
⁷⁸⁵ meaning a frequency of 40 MHz. Each recorded event by CMS has a nominal size
⁷⁸⁶ between 0.5 and 1 MB, corresponding to a data flow of around 10^9 MB/s = 1PB/s
⁷⁸⁷ that is extremely big for transfer and for storing. Therefore, an on-line selection
⁷⁸⁸ of events has to be done. The trigger system of CMS does this task in two fold,
⁷⁸⁹ a level 1 (L1) and a high level trigger (HLT). The L1 is hardware based and the
⁷⁹⁰ HLT is software based.

⁷⁹¹ From the searches conducted at CMS, the interesting events produced on proton-
⁷⁹² proton collisions for new physics searches are very rare. The enormous majority of
⁷⁹³ events coming from proton-proton collisions correspond to well understood phe-
⁷⁹⁴ nomena, while new physics events are 'exotic' with regards to the most common
⁷⁹⁵ type of events. Then it is interesting to keep only a part of the events, what
⁷⁹⁶ actually makes easier the analyses afterward done over the data.

⁷⁹⁷ The CMS trigger system is designed to keep only 100 kHz by the L1 and 300 Hz
⁷⁹⁸ by the HLT. L1 is reducing the data flux by 2 orders of magnitude and the HLT
⁷⁹⁹ another 3 orders of magnitude.

800 **Level 1 trigger**

801 The L1 is designed to trigger over coarse data coming from the calorimeters and
 802 muon chambers, holding data in pipe-lined memories in the front-end electronics.
 803 Therefore, relies on very fast reconstruction of objects coming from this subsystems:
 804 muons, electrons, photons, jets and missing energy. This reconstruction
 805 differs from the final reconstruction of the objects, for example a jet for the L1
 806 consists on successive energy deposits in the ECAL and HCAL, while the off-line
 807 reconstruction takes into account also the tracker information.

808 The L1 starts from regional data coming from the subsystems which is after-
 809 ward combined in order to build ranked trigger objects in localized regions of the
 810 detector. Global Muon and Calorimeter triggers sort the objects and send the best
 811 ranked to the Global Trigger (GT). Before the GT no events are rejected, it is only
 812 with the GT that the selection is applied. The GT combines the information and
 813 can apply topological requirements and take a decision on keeping or disregarding
 814 the event. On figure 2.21 can be found the work-flow of the L1.

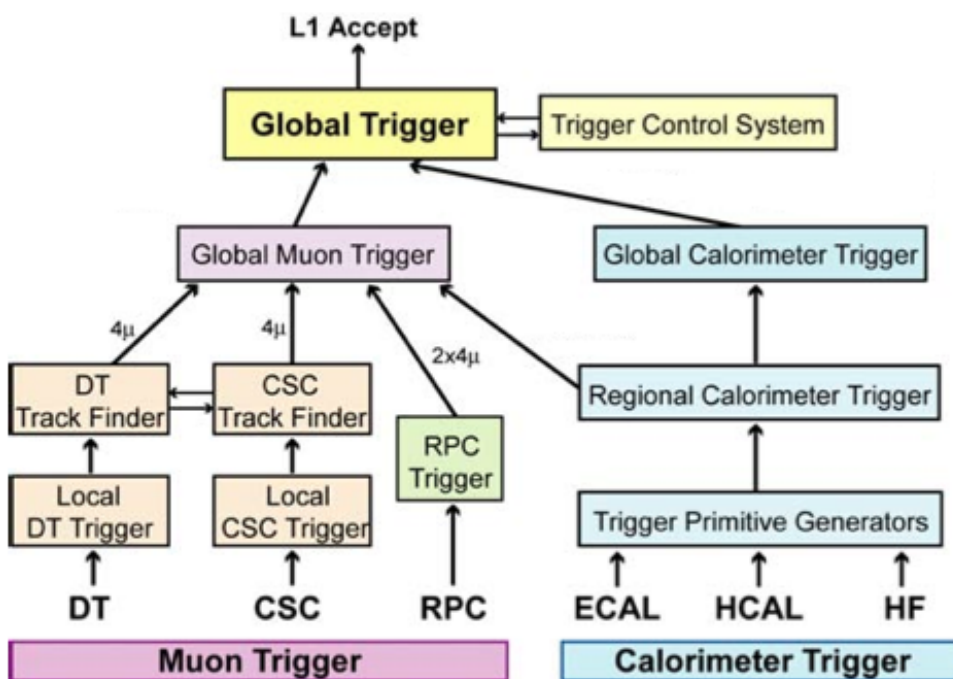


Figure 2.21: L1 architecture. ©CERN

815 The L1 cards are distributed between the detector and an adjoin cavern at 90
 816 m distance from the detector. The latency time that the L1 disposes between the

817 collision and the taking of the decision is about $3.2 \mu\text{s}$. Therefore, the front-end
818 memory in the cards should be able to keep in memory up to 128 bunch crossings.

819 **High Level Trigger**

820 The HLT takes as input the events accepted by the L1 and processes them using
821 farms of commercial processors. The HLT does additional operations on the se-
822 lected events making it much slower than L1 processing. In particular, the HLT
823 takes also into account the tracker information. Consequently, this system is able
824 to take into consideration the whole information of the detector. However, the
825 reconstruction of objects done by the HLT differs slightly from the final off-line
826 reconstruction. The decision taking process takes around 40 ms, 10^4 times more
827 than for L1.

828 The events selected by HLT are finally stocked on disks under several paths
829 depending on the selection performed. There is a constant development of HLT
830 paths focusing on different analysis requirements in order to obtain the best pos-
831 sible selection efficiency for specific signal types.

832 **2.3 Object reconstruction**

833 The different subsystems of CMS play specific roles in order to identify particles
834 from collisions and measure their properties. In order to achieve such measure-
835 ments, the information collected by the different parts of a subsystem should be
836 combined to reconstruct particle information. Also for some particles the infor-
837 mation between different subsystems should be connected to achieve a successful
838 identification. The easiest example is the reconstruction of tracks in the pixel de-
839 tector. In order to identify a track of a charged particle that traversed the pixel
840 barrel the hits of such particle in each layers should be considered at the same
841 time. A track in the pixel barrel is formed then by the three hits a particle leaves
842 in each barrel layer.

843 **2.3.1 Track and vertex reconstruction**

844 Track and vertices reconstruction in CMS are done by the tracker system.

845 **Vertex reconstruction**

846 Description of vertex reconstruction procedure.

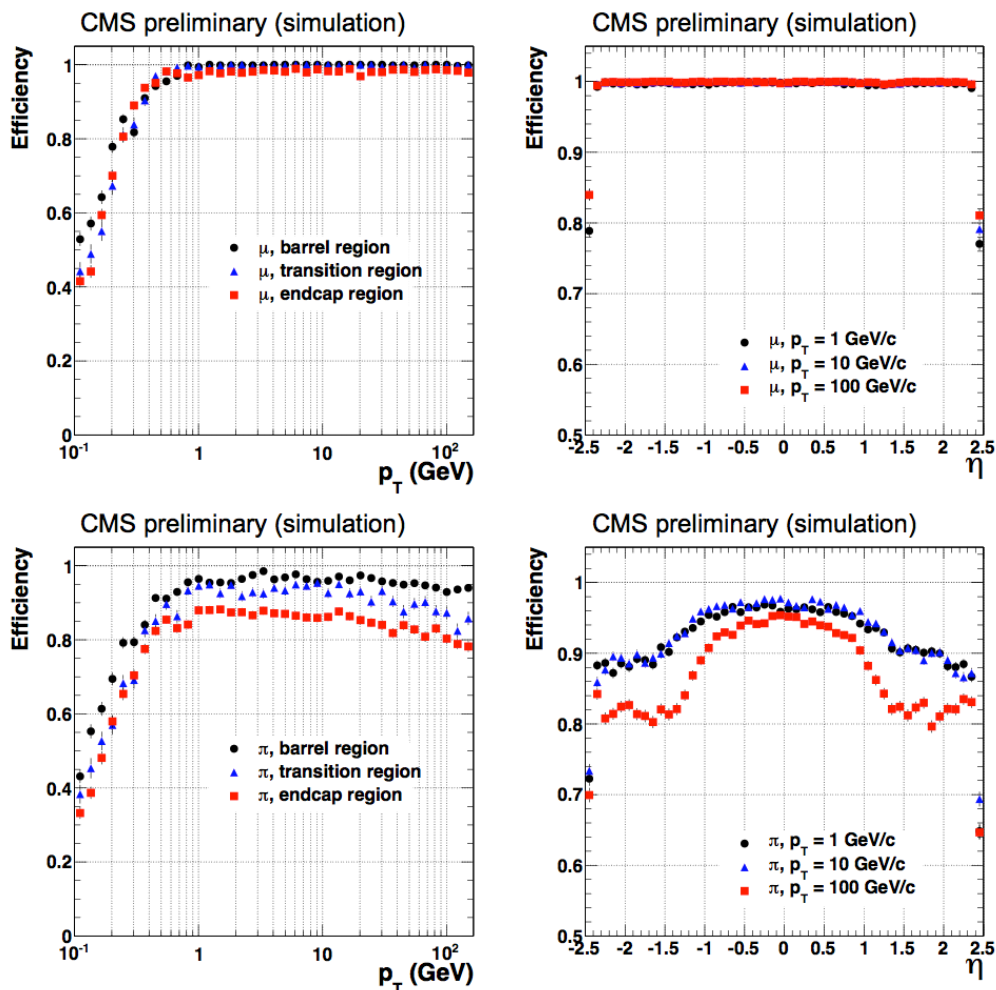


Figure 2.22:

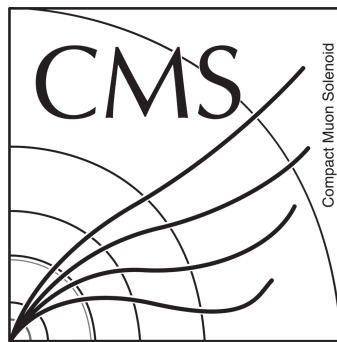


Figure 2.23: Resolution [left] and efficiency [right] of reconstruction of primary vertices.

⁸⁴⁷ 2.3.2 Particle Flow (PF) algorithm

⁸⁴⁸ Description of Particle flow algorithm.

⁸⁴⁹ Calorimeter clustering

⁸⁵⁰ Description on how calorimeter deposits are clustered for particle reconstruction.

⁸⁵¹ Subdetectors link

⁸⁵² How different subdetectors information are related to reconstruct different particles.
⁸⁵³

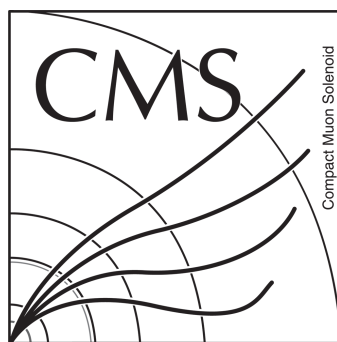


Figure 2.24: Connection between tracks reconstructed in the tracker (in green) and energy clusters in the ECAL [left] and HCAL clusters [right].

854 **2.3.3 Electron reconstruction**

855 Description of variables used to reconstruct electrons.

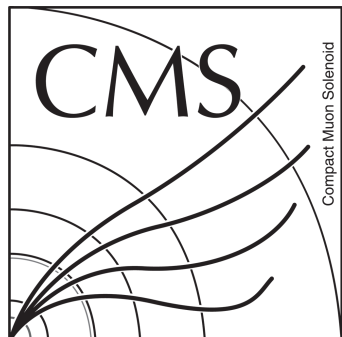


Figure 2.25: Reconstruction efficiency of electrons.

	xxxxxxx		xxxxxxx		xxxxxxx	
--	---------	--	---------	--	---------	--

Table 2.1: Identification requirements for electrons

856 **2.3.4 Muon reconstruction**

857 Muon reconstruction description and goodness of reconstruction from dimuon mass
858 spectra showing resonances.

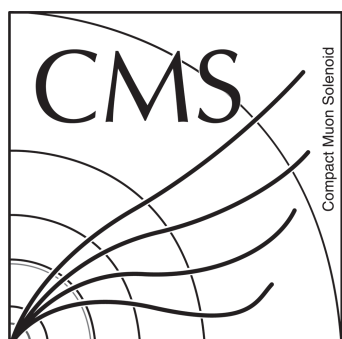


Figure 2.26: Reconstruction efficiency of muons.

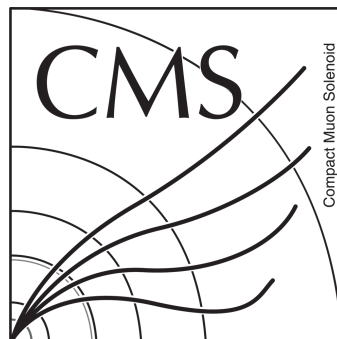


Figure 2.27: Dimuon mass spectra from reconstructed muons in CMS.

2.3.5 Jet reconstruction

Clustering algorithms

Description of basis of clustering algorithms.

SIScone SIScone algorithm definition. Characteristics discussion.

kT KT algorithm definition. Characteristics discussion.

Cambridge-Aachen CA algorithm definition. Characteristics discussion.

Anti-kT AK algorithm definition. Characteristics discussion.

Infrared and collinear safety Definition of infrared and collinear safety. Description of which algorithms are safe and why.

Jet area Jet area definition. Importance of jet area.

Jet energy corrections

Why jet energy corrections. Brief how.

JES description. JER description.

b-jets identification

Description of basic parameters that help to differentiate b-jets from light jets.

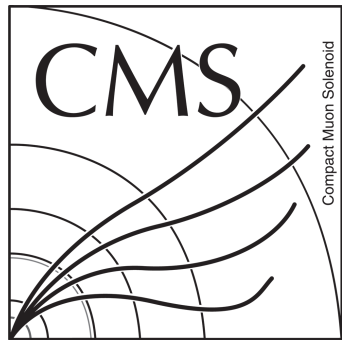


Figure 2.28: Jet areas for different jet algorithms related to the reconstructed p_T .



Figure 2.29: JEC uncertainties as function of p_T [left] and η [right].

- 874 **Identification algorithms and working points** Description of CSV algorithm.
875 Variables used. Efficiency of different working points.

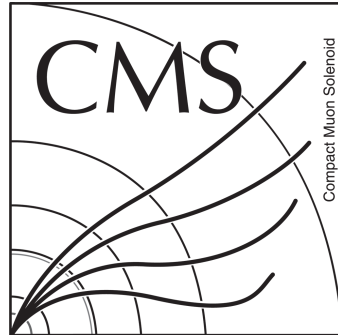


Figure 2.30: Number of secondary vertices [left] and CSV final discriminator variable [right] for each jet flavor.

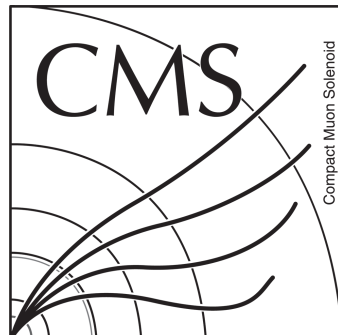


Figure 2.31: Efficiency of CSV b-tagging algorithm in the middle working point as function of jet p_T and η .

⁸⁷⁶ 3 Vector Like Quarks: Generic ⁸⁷⁷ model

⁸⁷⁸ From chapter 1 we have seen how there are some parts in the SM that does
⁸⁷⁹ not work very well. From such internal issues some further models/theories have
⁸⁸⁰ been developed. All this theories are commonly grouped under the term Beyond
⁸⁸¹ Standard Model or simply BSM. One of the most famous BSM theory is super-
⁸⁸² symmetry (SUSY). This theory postulates a symmetry that does not distinguish
⁸⁸³ between fermions and bosons. This idea have given birth to a plethora of model
⁸⁸⁴ realizations and physics predictions. So far, nothing of the new consequences of
⁸⁸⁵ this theory have been confirmed but the experiments have an enormous invest-
⁸⁸⁶ ment on their search. But not only SUSY have seen the day light, there is on the
⁸⁸⁷ market an astonishing amount of BSM theories addressing different issues of the
⁸⁸⁸ SM. Extra dimensions, fourth families, composite Higgs are a few of them.

⁸⁸⁹ In this chapter we will describe a bunch of models that introduce additional
⁸⁹⁰ heavy quarks, heavier than the top, in order to solve the hierarchy problem, de-
⁸⁹¹ scribed on section 1.5.

⁸⁹² 3.1 Motivation

- ⁸⁹³ Why to introduce extra quarks.
- ⁸⁹⁴ Plausible solution of hierarchy problem.
- ⁸⁹⁵ Reference to models with extra quarks. (?)

⁸⁹⁶ 3.2 Generic Formulation

⁸⁹⁷ Formalism: Generic Langranian. Description of mixings with SM quarks.

$$| \text{xxxxxx} | \text{xxxxxx} | \text{xxxxxx} |$$

Table 3.1: Possible VLQ representations and correponding $SU(2)_L \times U(1)$ charges.

3.2.1 Production modes

- 898 Description of pair and single production. Parallel to production modes of top.
900 Comparison between cross sections for pair and single production.

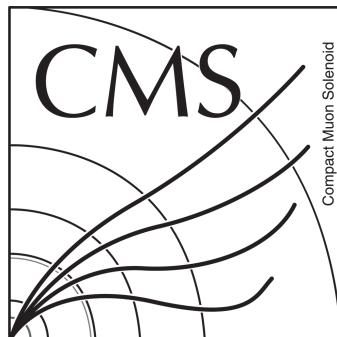


Figure 3.1: Feynman diagrams of T production in pairs [left] and single [right]

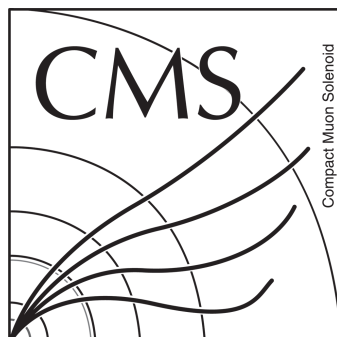


Figure 3.2: T production cross section for pair and single case as function of T mass for different center of mass energy in proton-proton collisions.

3.2.2 Decay modes

- 902 Description of possible decay channels of T . Relative importance of decay channels
903 depending on the mass.

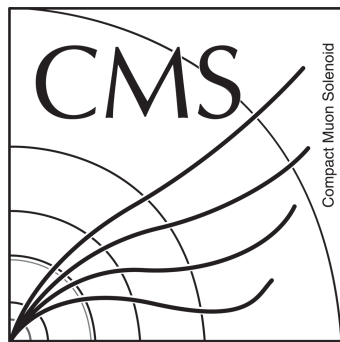


Figure 3.3: T branching ratios as function of its mass.

904 3.3 Fesability study for a search of a T at LHC at 8 905 TeV

906 Discussion on selection of full hadronic channel.

907 3.3.1 Stragey for the full hadronic final state

908 General discussion of strategy used for selection.

xxxxxxxx	xxxxxxxx	xxxxxxxx
----------	----------	----------

Table 3.2: Cross sections and expected number of events for background processes and signal.

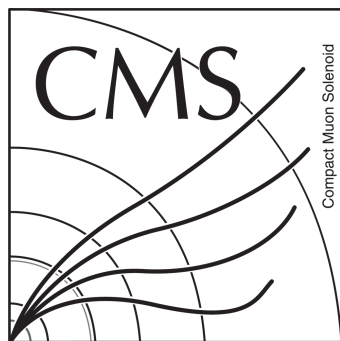


Figure 3.4: Forward jet produced in association with T .

₉₀₉ **3.3.2 Event selection**

₉₁₀ Description of selection. Paragraph per variable.

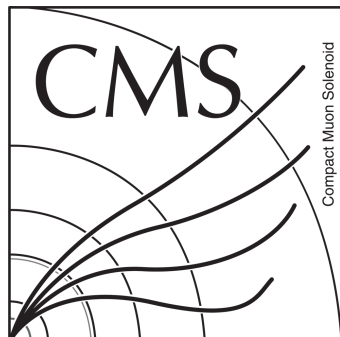


Figure 3.5: p_T of the six leading jets for backgrounds (stacked) and signal (over-imposed)

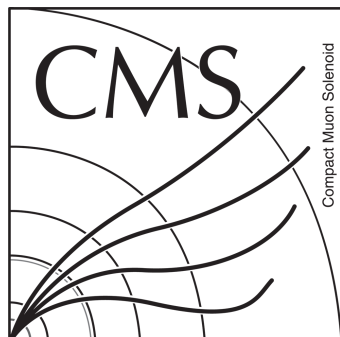


Figure 3.6: Total hadronic energy for backgrounds (stacked) and signal (over-imposed)

₉₁₁ **3.3.3 Results**

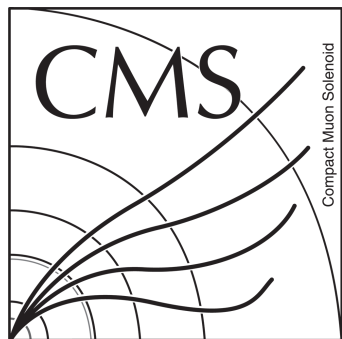


Figure 3.7: ΔR between the reconstructed Higgs and W for backgrounds (stacked) and signal (over-imposed)

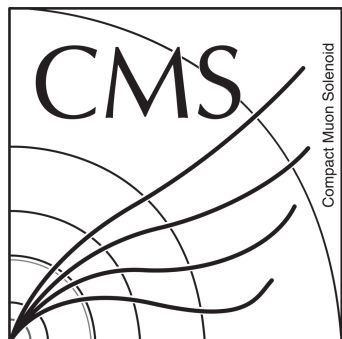


Figure 3.8: Mass of the reconstructed Higgs for backgrounds (stacked) and signal (over-imposed)

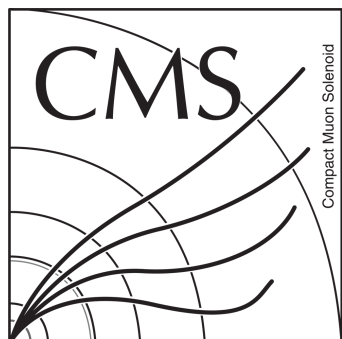


Figure 3.9: Relative total hadronic energy for backgrounds (stacked) and signal (over-imposed)

xxxxxxxx	xxxxxxxx	xxxxxxxx
----------	----------	----------

Table 3.3: Number of events for signal and backgrounds after the first selection cut (Cut 0), and efficiencies of each stage of the cutting procedure. The errors indicated are statistical only, based on the number of events.

	unweighted events after Cut 10	in mass window	weight	weighted events
Signal	8601	3780	0.03	113 ± 2
$t\bar{t}$	409	57	7.7	437 ± 58
$W+\text{jets}$	24	3	132	395 ± 228
QCD	235	34	6.48	220 ± 38
tW	18	3	11.3	34 ± 20
$t+\text{jet}$	75	7	3.55	25 ± 9
total background				1112 ± 352

Table 3.4: Number of signal and background events from our simulation: in the first column the simulated events that pass all kinematic cuts, in the second column the events that fall in the mass window $710 < M_{jjjj} < 750$ GeV, finally in the fourth column the number of weighted events in the mass window normalized to the physical cross section (the applied weight is listed in the third column). All the errors are statistical only. For the total background, we conservatively consider linear sum of errors.

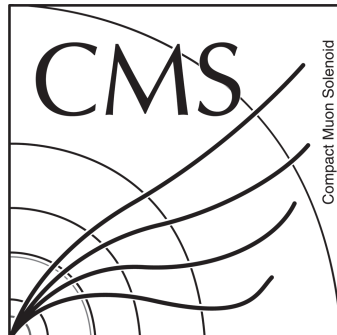


Figure 3.10: Reconstructed T mass after all cuts for backgrounds and signal (stacked)

912 4 Understanding theory predictions 913 via Monte-Carlo event generation

914 Although we have nowadays a very elegant and complete theoretical description
915 of particle physics, is not always evident how to translate this theory in actual
916 predictions, to compare with measurements. Moreover, on the case of hadronic
917 colliders, as the LHC, it's even more difficult due to the particularities of strong
918 interaction. On this subject, a set of tools and approaches have been developed in
919 order to be able to make accurate predictions from theory that could be directly
920 researched for on the experiments, as CMS or ATLAS for example. In the present
921 chapter, we describe such tools and formalisms and a set of studies comparing the
922 predictions these tools to data.

923 4.1 Mote-Carlo simulations

924 The Monte-Carlo simulations use random numbers and large samplings to calcu-
925 late mathematical quantities in complex configurations, as integrals or probabili-
926 ties. The typical example is on how to calculate the integral of a one-dimensional
927 function. One can throw several random coordinates pair in the Cartesian plane
928 and count how many of them are under the function. Then the integral of the
929 function will be proportional to the fraction of points under the curve to the total
930 thrown points. Larger the number of points, closer the estimation to the real value.
931 An illustration of the procedure can be seen in figure 4.1.

932 A similar method is used to simulate proton-proton collisions. This simulation is
933 used to generate “random” events and to calculate quantities, as the cross section,
934 for a given physical process. Each event represent the final state of a collision, i.e.
935 the set of particles produced from the collision and seen by a detector. Such simu-
936 lations comprehend different stages: first, the partonic processes making reference
937 to the interaction between the partons inside the proton; second, the hadroniza-
938 tion of the particles produce from parton interactions; and third, the simulation of
939 the interaction between the hadrons (from second step) and the detector material.
940 Such events are used to evaluate predictions from theory in the frame of a specific
941 experiment. Whereas the hadronization and detector simulation are well-known
942 physical processes, new theories predictions rely basically on the partonic level,

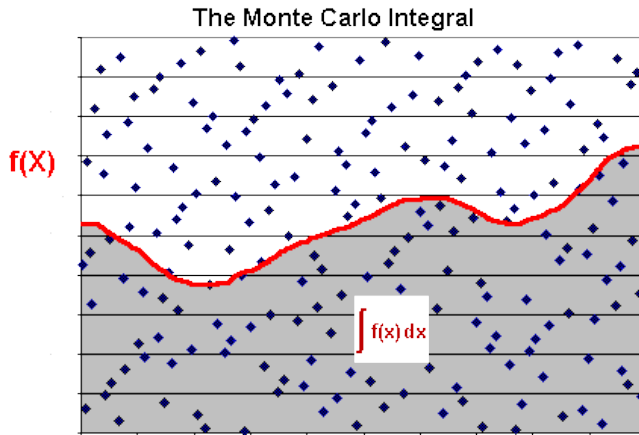


Figure 4.1: Integration using Monte-Carlo methods

943 where the fundamental interaction processes take part.

944 4.1.1 Parton simulation

945 The parton model was initially proposed by Richard Feynman in 1969, as a method
 946 to understand collisions of non-fundamental particles. The model consider a non-
 947 fundamental particle, as a proton or a neutron, composed of a given number of
 948 point-like fundamental particles. When a collision occur the point-like particles
 949 inside have a major probability to scatter. For example, when an electron is fired
 950 against a proton the most of the interactions will between the electron and the
 951 fundamental components of the proton, u and d quarks. This “hard” components
 952 are called *valence* quarks. Surrounding them there are the *sea* quarks and gluons.

953 However, as the energy of the collision increases the probability to scatter a sea
 954 component, quark or gluon, increases. In addition, even if the valence quarks of a
 955 proton are the u and d quarks, heavier quarks can appear in the sea, as the b , c or s
 956 quarks. The probability to interact with a component, valence or sea, is described
 957 by parton distribution function, commonly called PDF. A PDF $f \equiv f(x, Q^2)$ rep-
 958 resent the number density of a given quark or gluon as a function of the energy
 959 scale Q^2 and the fraction of momentum carried by the parton x . The determina-
 960 tion of a PDF is done via a fit of large data samples from experiments specifically
 961 designed to test the inner structure of nucleons. The DIS (Deep Inelastic Scat-
 962 tering) experiment at SLAC (Stanford Linear Accelerator Center), in California,
 963 United States, first probed the existence of partonic structure inside nucleons us-
 964 ing leptons as probes scattered against nucleons. Another important experiment
 965 was the HERA accelerator at DESY in Hamburg, Germany, which used electrons

966 to study the inner structure of protons.

967 In figure 4.2 is shown the Martin-Stirling-Thorne-Watt [18] (MSTW) PDF for
 968 two energy scales. The MSTW PDF is one of the experimental fits combining data
 969 from DIS and HERA. In this PDF can be seen that u and d quarks carry the most
 970 of the momentum of the proton. The rest of the momentum is spread mainly over
 971 a huge amount of gluons and some, less probable, sea quarks as \bar{u}, \bar{d} or c and s .
 972 One important feature is that the composition of the proton changes depending
 973 on the energy scale. At $Q^2 = 10 \text{ GeV}^2$ there is no b -quark in the proton while at
 974 $Q^2 = 10^4 \text{ GeV}^2$ there is a non-negligible probability to find it in the proton.

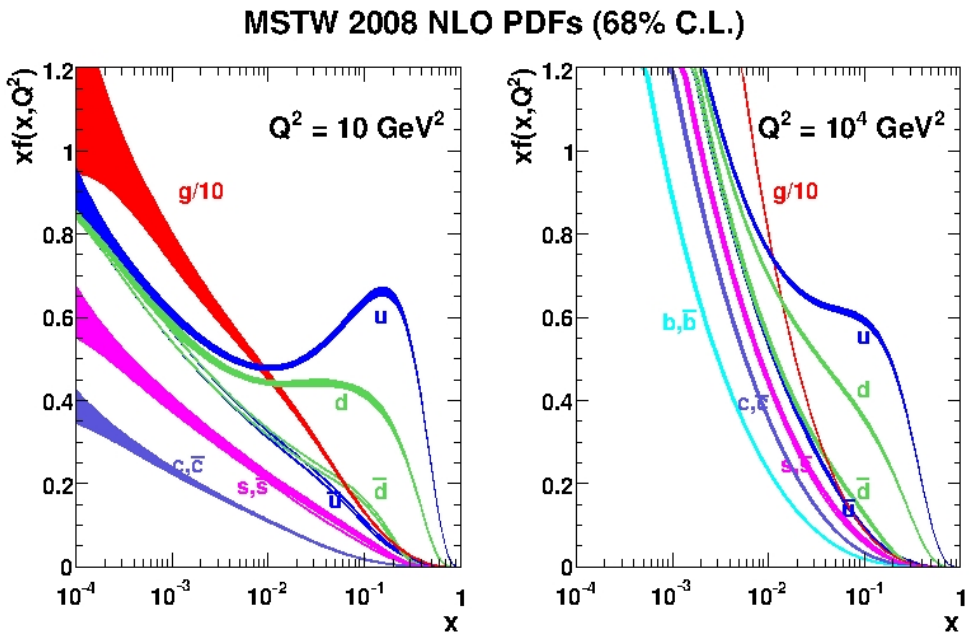


Figure 4.2: Martin-Stirling-Thorne-Watt proton PDF for $Q^2 = 10 \text{ GeV}^2$ [left] and $Q^2 = 10^4 \text{ GeV}^2$ [right]. From [18]

975 Two other important PDF fits are CTEQ [19] and NNPDF [20]. Together with
 976 MSTW, they are the most used PDF sets in the CMS experiment for MC produc-
 977 tion.

978 For the hard process, the differential cross section can be written as,

$$\begin{aligned}
d\sigma_{ij \rightarrow lm} &= \left(\int_0^1 \int_0^1 f_i(x_i, Q^2) f_j(x_j, Q^2) dx_i dx_j \right) \\
&\times \frac{d^3 p_l}{(2\pi)^2 2E_l} \frac{d^3 p_m}{(2\pi)^2 2E_m} \delta^4(p_i + p_j - p_l - p_m) \\
&\times |\mathcal{M}_{ij \rightarrow lm}|^2
\end{aligned} \tag{4.1}$$

where $f_{i,j}$ correspond to the PDF's of the initial partons. $\mathcal{M}_{ij \rightarrow lm}$ is the matrix element of the process which is the part of the S-matrix that contains the amplitude of the process, and modules the transition from the initial to the final state [21]. The matrix element could account effectively for all processes mediating the transition from the initial to the given final state, but in practice it is calculated only including a given number of processes. The calculation can achieve different levels, usually tree level or Leading Order (LO), but modern calculation could arrive, depending on the process, to one loop or Next-to-Leading-Order (NLO) or even two loops the Next-to-Next-to-Leading-Order (NNLO). This limit depends exclusively on the feasibility of the theoretical calculations. In figure 4.3 is shown an example of a leading order plus its corresponding NLO diagrams for a fermion scattering.

4.1.2 Hadron simulation

■ Figure to illustrate to hadronization process ■

4.1.3 Detector simulation

4.2 Tools

4.2.1 Matrix-element generators

4.2.2 Hadron generators

4.3 Validation on data

■ Plot of W+jets and Z+jets comparison between data and MC for a set of different generators. Plot on top pt to briefly introduce tpo pt reweighting ■

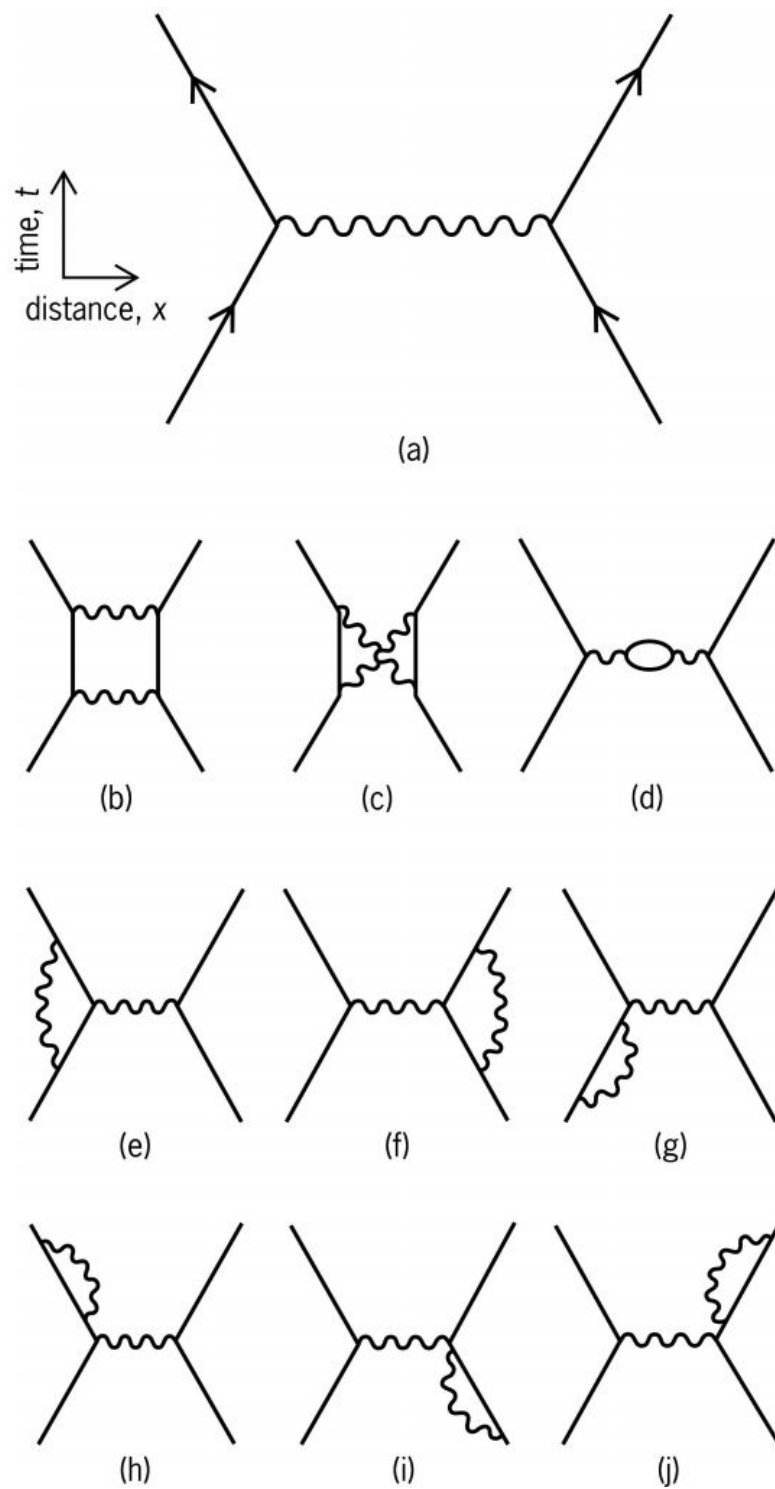


Figure 4.3: LO (a) and NLO (b)-(j) processes contributing to fermions scattering

1002 **5 Search for a single produced T'**
1003 **decaying into top and Higgs in**
1004 **the full hadronic final state**

1005 In the present chapter we describe in full detail the search performed using 2012
1006 data collected by CMS for a T' in the full hadronic final state. The theoretical
1007 formalism for such object has been described on chapter 3.

1008 **5.1 Analysis Strategy**

1009 **5.2 Datasets**

1010 ■ Table with Multijet primary
1011 datasets and integrated luminosity. Tables
1012 for MC samples, backgrounds and signal
1013 mass points. ■

1014 **5.3 Event selection**

1015 **5.3.1 Event processing**

1016 **5.3.2 Basic selection**

1017 ■ Plots of pt and eta
1018 of six leading jets, number of vertices, HT
1019 and number of CSV b-tagged jets ■

1020 **5.3.3 T' reconstruction with a χ^2 sorting algorithm**

1021 ■ Table with inclusive and exclusive
1022 reconstruction efficiency. Plots of mass of
1023 reconstructed T, W, H and top right after
1024 reconstruction for all mass points. Table
1025 with gaussian fit results. ■

1026 **5.3.4 Selection based on reconstructed objects**

1027 ■ $N - 1$ plots for object selection variables.
1028 Table with S/B and $S/\sqrt{S + B}$ from MC
1029 for each step of the selection. ■

1030 **5.3.5 Efficiencies**

1031 **Trigger**

1032 ■ Trigger efficiency plots ■

1033 **Selection**

1034 ■ Table with efficiencies of full
1035 selection. Plot with selection efficiency for
1036 all mass points. ■

1037 **5.4 Background estimation from data**

1038 **5.4.1 Known difficulties and tried methods**

1039 ■ 2D plot of $pT(H)$
1040 and $pT(\text{top})$ to show correlation and ta-
1041 ble with ttbar+QCD and signal content in

₁₀₄₂ each region from ABCD method based on
₁₀₄₃ $pT(H)$ and $pT(\text{top})$

■

₁₀₄₄ **5.4.2 Method**

₁₀₄₅ **5.4.3 Validation**

₁₀₄₆ ■ Validation plots: MC, Data. Chi2
₁₀₄₇ plots for minimization. Number of com-
₁₀₄₈ binations in the control sample plot. Plot
₁₀₄₉ of M_{5J} for different values of chi2. Ta-
₁₀₅₀ ble with signal contamination percentage
₁₀₅₁ in the control sample cut per cut and for
₁₀₅₂ all mass points.

■

₁₀₅₃ **5.5 Systematics**

₁₀₅₄ ■ Tables for PDF, b-tagging and JEC
₁₀₅₅ systematics. Table with full systematics. ■

₁₀₅₆ **5.6 Results**

₁₀₅₇ ■ Expected and observed yields table.
₁₀₅₈ Exclusion limits plot. M_{5J} plot for data
₁₀₅₉ with estimated background and signal. ■

1060

Bibliography

- 1061 [1] O. S. Brüning, P. Collier, P. Lebrun, S. Myers, R. Ostoja, J. Poole, and
1062 P. Proudlock, *LHC Design Report*. CERN, Geneva, 2004.
- 1063 [2] **CMS Collaboration** Collaboration, G. L. Bayatian *et al.*, *CMS Physics:*
1064 *Technical Design Report Volume 1: Detector Performance and Software*.
1065 Technical Design Report CMS. CERN, Geneva, 2006. There is an error on
1066 cover due to a technical problem for some items.
- 1067 [3] **CMS Collaboration** Collaboration, G. L. Bayatian *et al.*, “CMS Physics:
1068 Technical Design Report Volume 2: Physics Performance,” *J. Phys. G* **34**
1069 no. CERN-LHCC-2006-021. CMS-TDR-8-2, (2007) 995–1579. 669 p. revised
1070 version submitted on 2006-09-22 17:44:47.
- 1071 [4] **ATLAS Collaboration** Collaboration, A. Collaboration, *ATLAS detector
1072 and physics performance: Technical Design Report*. Technical Design Report
1073 ATLAS. CERN, Geneva, 1999. Electronic version not available.
- 1074 [5] **LHCb Collaboration** Collaboration, J. Alves, A. Augusto *et al.*, “The
1075 LHCb Detector at the LHC,” *JINST* **3** (2008) S08005.
- 1076 [6] **ALICE Collaboration** Collaboration, P. Cortese, C. W. Fabjan,
1077 L. Riccati, K. Safarík, and H. de Groot, *ALICE physics performance:
1078 Technical Design Report*. Technical Design Report ALICE. CERN, Geneva,
1079 2005. revised version submitted on 2006-05-29 15:15:40.
- 1080 [7] **UA4/2 Collaboration** Collaboration, C. Augier *et al.*, “Predictions on the
1081 total cross-section and real part at LHC and SSC,” *Phys.Lett.* **B315** (1993)
1082 503–506.
- 1083 [8] C. Mathis, T. Bhattacharya, and S. Imari Walker, “The Emergence of Life
1084 as a First Order Phase Transition,” *ArXiv e-prints* (Mar., 2015) ,
1085 arXiv:1503.02776 [nlin.AO].
- 1086 [9] F. Jegerlehner, “The hierarchy problem of the electroweak Standard Model
1087 revisited,” arXiv:1305.6652 [hep-ph].

- 1088 [10] S. P. Martin, “A Supersymmetry primer,” *Adv.Ser.Direct.High Energy Phys.*
 1089 **21** (2010) 1–153, [arXiv:hep-ph/9709356 \[hep-ph\]](#).
- 1090 [11] **CMS** Collaboration, V. Khachatryan *et al.*, “Search for neutral MSSM
 1091 Higgs bosons decaying to a pair of tau leptons in pp collisions,” *JHEP* **1410**
 1092 (2014) 160, [arXiv:1408.3316 \[hep-ex\]](#).
- 1093 [12] **ATLAS** Collaboration, G. Aad *et al.*, “Search for neutral Higgs bosons of
 1094 the minimal supersymmetric standard model in pp collisions at $\sqrt{s} = 8$ TeV
 1095 with the ATLAS detector,” *JHEP* **1411** (2014) 056, [arXiv:1409.6064 \[hep-ex\]](#).
- 1096 [13] **Super-Kamiokande** Collaboration, Y. Ashie *et al.*, “Evidence for an
 1097 oscillatory signature in atmospheric neutrino oscillation,” *Phys.Rev.Lett.* **93**
 1098 (2004) 101801, [arXiv:hep-ex/0404034 \[hep-ex\]](#).
- 1100 [14] C. Weinheimer and K. Zuber, “Neutrino Masses,” *Annalen Phys.* **525**
 1101 no. 8-9, (2013) 565–575, [arXiv:1307.3518](#).
- 1102 [15] C. L. Bennett, D. Larson, J. L. Weiland, N. Jarosik, G. Hinshaw,
 1103 N. Odegard, K. M. Smith, R. S. Hill, B. Gold, M. Halpern, E. Komatsu,
 1104 M. R. Nolta, L. Page, D. N. Spergel, E. Wollack, J. Dunkley, A. Kogut,
 1105 M. Limon, S. S. Meyer, G. S. Tucker, and E. L. Wright, “Nine-year
 1106 Wilkinson Microwave Anisotropy Probe (WMAP) Observations: Final Maps
 1107 and Results,” *The Astrophysical Journal, Supplement* **208** (Oct., 2013) 20,
 1108 [arXiv:1212.5225 \[astro-ph.CO\]](#).
- 1109 [16] G. Hinshaw, D. Larson, E. Komatsu, D. N. Spergel, C. L. Bennett,
 1110 J. Dunkley, M. R. Nolta, M. Halpern, R. S. Hill, N. Odegard, L. Page,
 1111 K. M. Smith, J. L. Weiland, B. Gold, N. Jarosik, A. Kogut, M. Limon, S. S.
 1112 Meyer, G. S. Tucker, E. Wollack, and E. L. Wright, “Nine-year Wilkinson
 1113 Microwave Anisotropy Probe (WMAP) Observations: Cosmological
 1114 Parameter Results,” *The Astrophysical Journal, Supplement* **208** (Oct.,
 1115 2013) 19, [arXiv:1212.5226 \[astro-ph.CO\]](#).
- 1116 [17] **Planck** Collaboration, P. Ade *et al.*, “Planck 2015 results. XIII.
 1117 Cosmological parameters,” [arXiv:1502.01589 \[astro-ph.CO\]](#).
- 1118 [18] A. Martin, W. Stirling, R. Thorne, and G. Watt, “Parton distributions for
 1119 the LHC,” *Eur.Phys.J.* **C63** (2009) 189–285, [arXiv:0901.0002 \[hep-ph\]](#).
- 1120 [19] P. M. Nadolsky, H.-L. Lai, Q.-H. Cao, J. Huston, J. Pumplin, *et al.*,
 1121 “Implications of CTEQ global analysis for collider observables,” *Phys.Rev.*
 1122 **D78** (2008) 013004, [arXiv:0802.0007 \[hep-ph\]](#).

- 1123 [20] R. D. Ball, L. Del Debbio, S. Forte, A. Guffanti, J. I. Latorre, *et al.*, “A first
1124 unbiased global NLO determination of parton distributions and their
1125 uncertainties,” *Nucl.Phys.* **B838** (2010) 136–206, arXiv:1002.4407
1126 [[hep-ph](#)].
- 1127 [21] M. E. Peskin and D. V. Schroeder, *An introduction to quantum field theory*.
1128 Advanced book program. Westview Press Reading (Mass.), Boulder (Colo.),
1129 1995. <http://opac.inria.fr/record=b1131978>. Autre tirage : 1997.

Contents

1131	1 The Standard Model	5
1132	1.1 Fields, symmetries and interactions	6
1133	1.2 Quantum fields and particles	8
1134	1.2.1 The mass problem	10
1135	1.2.2 Spontaneous Symmetry Breaking	11
1136	1.2.3 Englert-Brout-Higgs mechanism	12
1137	1.3 Top production at LHC	13
1138	1.3.1 Pair production	14
1139	1.3.2 Single t production	14
1140	1.3.3 Decay channels	14
1141	1.3.4 Top properties	14
1142	1.4 Higgs production at LHC	18
1143	1.4.1 Decay channels	19
1144	1.4.2 Higgs properties	19
1145	1.5 Hierarchy problem and other limitations	19
1146	2 The CMS experiment at LHC	25
1147	2.1 The Large Hadron Collider	25
1148	2.1.1 Injector chain	26
1149	2.1.2 Main ring	28
1150	2.1.3 Run 1	31
1151	2.1.4 Other experiments at LHC	32
1152	2.2 The Compact Muon Solenoid (CMS) experiment	34
1153	2.2.1 Coordinate system	37
1154	2.2.2 Magnet	39
1155	2.2.3 Tracker system	40
1156	2.2.4 Electromagnetic calorimeter	42
1157	2.2.5 Hadronic Calorimeter	45
1158	2.2.6 Muon chambers	46
1159	2.2.7 Trigger	48
1160	2.3 Object reconstruction	50
1161	2.3.1 Track and vertex reconstruction	50
1162	2.3.2 Particle Flow (PF) algorithm	52

1163	2.3.3	Electron reconstruction	53
1164	2.3.4	Muon reconstruction	53
1165	2.3.5	Jet reconstruction	54
1166	3	VLQ models	57
1167	3.1	Motivation	57
1168	3.2	Generic Formulation	57
1169	3.2.1	Production modes	58
1170	3.2.2	Decay modes	58
1171	3.3	Fesability study for a search of a T at LHC at 8 TeV	59
1172	3.3.1	Stragey for the full hadronic final state	59
1173	3.3.2	Event selection	60
1174	3.3.3	Results	60
1175	4	MC event generation	63
1176	4.1	Mote-Carlo simulations	63
1177	4.1.1	Parton simulation	64
1178	4.1.2	Hadron simulation	66
1179	4.1.3	Detector simulation	66
1180	4.2	Tools	66
1181	4.2.1	Matrix-element generators	66
1182	4.2.2	Hadron generators	66
1183	4.3	Validation on data	66
1184	5	Single VLQ search	69
1185	5.1	Analysis Strategy	69
1186	5.2	Datasets	69
1187	5.3	Event selection	69
1188	5.3.1	Event processing	69
1189	5.3.2	Basic selection	69
1190	5.3.3	T' reconstruction with a χ^2 sorting algorithm	70
1191	5.3.4	Selection based on reconstructed objects	70
1192	5.3.5	Efficiencies	70
1193	5.4	Background estimation from data	70
1194	5.4.1	Known difficulties and tried methods	70
1195	5.4.2	Method	71
1196	5.4.3	Validation	71
1197	5.5	Systematics	71
1198	5.6	Results	71